

This copy is for your personal, non-commercial use only.

If you wish to distribute this article to others, you can order high-quality copies for your colleagues, clients, or customers by [clicking here](#).

Permission to republish or repurpose articles or portions of articles can be obtained by following the guidelines [here](#).

The following resources related to this article are available online at www.sciencemag.org (this information is current as of May 11, 2014):

Updated information and services, including high-resolution figures, can be found in the online version of this article at:

<http://www.sciencemag.org/content/344/6184/634.full.html>

Supporting Online Material can be found at:

<http://www.sciencemag.org/content/suppl/2014/04/09/science.1252826.DC1.html>

A list of selected additional articles on the Science Web sites **related to this article** can be found at:

<http://www.sciencemag.org/content/344/6184/634.full.html#related>

This article **cites 38 articles**, 9 of which can be accessed free:

<http://www.sciencemag.org/content/344/6184/634.full.html#ref-list-1>

This article has been **cited by** 1 articles hosted by HighWire Press; see:

<http://www.sciencemag.org/content/344/6184/634.full.html#related-urls>

This article appears in the following **subject collections**:

Neuroscience

<http://www.sciencemag.org/cgi/collection/neuroscience>

References and Notes

1. Q. Shen *et al.*, *Science* **304**, 1338–1340 (2004).
2. M. Tavazoie *et al.*, *Cell Stem Cell* **3**, 279–288 (2008).
3. T. Shingo *et al.*, *Science* **299**, 117–120 (2003).
4. P. Wu *et al.*, *Neurobiol. Aging* **29**, 1502–1511 (2008).
5. H. van Praag, G. Kempermann, F. H. Gage, *Nat. Neurosci.* **2**, 266–270 (1999).
6. J. S. Snyder, A. Soumier, M. Brewer, J. Pickel, H. A. Cameron, *Nature* **476**, 458 (2011).
7. E. Farkas, P. G. Luiten, *Prog. Neurobiol.* **64**, 575–611 (2001).
8. H. G. Kuhn, H. Dickinson-Anson, F. H. Gage, *J. Neurosci.* **16**, 2027–2033 (1996).
9. T. Seki, Y. Arai, *Neuroreport* **6**, 2479–2482 (1995).
10. S. A. Villeda *et al.*, *Nature* **477**, 90–94 (2011).
11. J. M. Ruckh *et al.*, *Cell Stem Cell* **10**, 96–103 (2012).
12. V. E. Miron *et al.*, *Nat. Neurosci.* **16**, 1211–1218 (2013).
13. F. S. Loffredo *et al.*, *Cell* **153**, 828–839 (2013).
14. D. E. Wright, A. J. Wagers, A. P. Gulati, F. L. Johnson, I. L. Weissman, *Science* **294**, 1933–1936 (2001).
15. T. Seki, *J. Neurosci. Res.* **70**, 327–334 (2002).
16. A. García, B. Steiner, G. Kronenberg, A. Bick-Sander, G. Kempermann, *Aging Cell* **3**, 363–371 (2004).
17. J. Luo, S. B. Daniels, J. B. Lenington, R. Q. Notti, J. C. Conover, *Aging Cell* **5**, 139–152 (2006).
18. V. Tropepe, C. G. Craig, C. M. Morshead, D. van der Kooy, *J. Neurosci.* **17**, 7850–7859 (1997).
19. B. A. Reynolds, S. Weiss, *Science* **255**, 1707–1710 (1992).
20. L. Katsimpardi *et al.*, *Stem Cells* **26**, 1796–1807 (2008).
21. A. Carleton, L. T. Petreanu, R. Lansford, A. Alvarez-Buylla, P. M. Lledo, *Nat. Neurosci.* **6**, 507–518 (2003).
22. R. M. Witt, M. M. Galligan, J. R. Despinoy, R. Segal, *J. Vis. Exp.* **28**, 949 (2009).
23. M. J. Reed, J. M. Edelberg, *Sci. SAGE KE* **2004**, pe7 (2004).
24. A. Rivard *et al.*, *Circulation* **99**, 111–120 (1999).
25. D. R. Riddle, W. E. Sonntag, R. J. Lichtenwalner, *Ageing Res. Rev.* **2**, 149–168 (2003).
26. C. L. Grady *et al.*, *Neuroimage* **8**, 409–425 (1998).
27. R. Balabanov, P. Dore-Duffy, *J. Neurosci. Res.* **53**, 637–644 (1998).
28. P. Carmeliet, *Nat. Rev. Genet.* **4**, 710–720 (2003).
29. A. Alvarez-Buylla, D. A. Lim, *Neuron* **41**, 683–686 (2004).
30. M. Brines, A. Cerami, *Nat. Rev. Neurosci.* **6**, 484–494 (2005).
31. E. R. Matarredona, M. Murillo-Carretero, B. Moreno-López, C. Estrada, *Brain Res. Brain Res. Rev.* **49**, 355–366 (2005).
32. M. Sinha *et al.*, *Science* **344**, 649–652 (2014).

Acknowledgments: We thank C. McGillivray and D. Faria at the HSCRB Histology Core for providing help with sectioning

and D. Smith and B. Götzte at the HCBI for providing microscope facilities. We also thank W. Stallcup for providing the anti-NG2 antibody, C. Bonal for technical help and J. LaLonde for editorial assistance. This work was supported by a Senior Scholar in Aging Award from The Ellison Medical Foundation to L.L.R.; awards from GlaxoSmithKline and the Harvard Stem Cell Institute to L.L.R.; NIH (R01 AG032977 1R01 AG040019) to R.T.L.; and the Paul F. Glenn Foundation for Medical Research, NIH (1R01 AG033053, 1DP2 OD004345, and SU01 HL100402), and Harvard Stem Cell Institute to A.J.W. Additional data are in the Supplement. J.C. was funded by NIH R01NS070835 and R01NS072167. L.L.R., A.J.W., R.T.L., and L.K. are inventors on a U.S. patent application filed by Harvard University and Brigham and Women's Hospital entitled "Methods and Compositions for Increasing Neurogenesis and Angiogenesis" (61/833,813).

Supplementary Materials

www.sciencemag.org/content/344/6184/630/suppl/DC1
Materials and Methods

Figs. S1 to S12

References (33–34)

22 January 2014; accepted 10 April 2014
10.1126/science.1251141

Identification of LRRC8 Heteromers as an Essential Component of the Volume-Regulated Anion Channel VRAC

Felizia K. Voss,^{1,2,3} Florian Ullrich,^{1,2,3} Jonas Münch,^{1,2,3} Katina Lazarow,¹ Darius Lutter,^{1,2,3} Nancy Mah,² Miguel A. Andrade-Navarro,² Jens P. von Kries,¹ Tobias Stauber,^{1,2,*} Thomas J. Jentsch^{1,2,4*}

Regulation of cell volume is critical for many cellular and organismal functions, yet the molecular identity of a key player, the volume-regulated anion channel VRAC, has remained unknown. A genome-wide small interfering RNA screen in mammalian cells identified LRRC8A as a VRAC component. LRRC8A formed heteromers with other LRRC8 multspan membrane proteins. Genomic disruption of LRRC8A ablated VRAC currents. Cells with disruption of all five LRRC8 genes required LRRC8A cotransfection with other LRRC8 isoforms to reconstitute VRAC currents. The isoform combination determined VRAC inactivation kinetics. Taurine flux and regulatory volume decrease also depended on LRRC8 proteins. Our work shows that VRAC defines a class of anion channels, suggests that VRAC is identical to the volume-sensitive organic osmolyte/anion channel VSOAC, and explains the heterogeneity of native VRAC currents.

Cells regulate their volume to counteract swelling or shrinkage caused by osmotic challenges and during processes such as cell growth, division, and migration. As water transport across cellular membranes is driven by osmotic gradients, cell volume regulation requires appropriate changes of intracellular concentrations of ions or organic osmolytes such as taurine (1, 2). Regulatory volume decrease (RVD) follows the extrusion of intracellular Cl⁻ and K⁺ and other osmolytes across the plasma membrane. A key player is the volume-regulated anion channel VRAC that mediates character-

istic swelling-activated Cl⁻ currents [$I_{Cl(swell)}$] and is ubiquitously expressed in vertebrate cells (3–5). Nearly inactive under resting conditions, VRAC slowly opens upon hypotonic swelling. The mechanism behind VRAC opening remains enigmatic. VRAC currents are outwardly rectifying [hence the alternative name VSOR for volume-stimulated outward rectifier (4, 5)] and show variable inactivation at inside-positive voltages. VRAC conducts iodide (I⁻) better than chloride (Cl⁻) and might also conduct organic osmolytes such as taurine (6) [hence VSOAC, volume-stimulated organic osmolyte/anion channel (7)], but this notion is controversial (8–10). VRAC is believed to be important for cell volume regulation and swelling-induced exocytosis (11) and also for cell cycle regulation, proliferation, and migration (1, 3, 4). It may play a role in apoptosis and various pathological states, including ischemic

brain edema and cancer (4, 12). Progress in the characterization of VRAC and its biological roles has been limited by the failure to identify the underlying protein(s) despite decades of efforts (1, 5). Cl⁻ channels activate upon cell swelling, but their inward rectification and Cl⁻ over I⁻ selectivity deviate from VRAC (13). *Drosophila* dBest1, a member of a family of Ca²⁺-activated Cl⁻ channels, mediates swelling-activated Cl⁻ currents in insect cells (14, 15), but their characteristics differ from those of VRAC currents, and the mammalian homolog of dBest1 is swelling-insensitive (16). We show that VRAC represents a distinct class of anion channels that also conduct organic osmolytes.

To identify VRAC, we used a genome-wide RNA interference screen that could identify non-redundant VRAC components. Swelling-induced I⁻ influx into human embryonic kidney (HEK) cells expressing the I⁻-sensitive yellow fluorescent protein YFP(H148Q/I152L) (17) was used as readout in a fluorometric imaging plate reader (Fig. 1A). Exposure to saline containing 50 mM I⁻ yielded a slow fluorescence decay under isotonic conditions, whereas hypotonicity induced a delayed increase in YFP quenching (Fig. 1B) that could be reduced by VRAC inhibitors such as carbenoxolone (18) (fig. S1). In a prescreen targeting 21 anion transporters (table S1), only small interfering RNAs (siRNAs) against the Cl⁻/HCO₃⁻ exchanger AE2 gave significant effects (Fig. 1B). They decreased I⁻ influx under both isotonic and hypotonic conditions.

Our genome-wide screen used three separately transfected siRNAs per gene (fig. S2). Offline data analysis (fig. S3, A and B) yielded the maximal slope of fluorescence quenching that was used to define hits. Further criteria included the presence of predicted transmembrane domains and a wide expression pattern. Eighty-seven genes (table S2) were taken into a secondary screen with independent siRNAs. Of these, only sup-

¹Leibniz-Institut für Molekulare Pharmakologie (FMP), Berlin. ²Max-Delbrück-Centrum für Molekulare Medizin (MDC), Berlin. ³Graduate Program of the Freie Universität Berlin. ⁴Neurocare, Charité Universitätsmedizin, Berlin.

*Corresponding author. E-mail: jentsch@fmp-berlin.de (T.J.J.); tstauber@fmp-berlin.de (T.S.)

pression of leucine-rich repeat-containing 8A (LRRC8A) robustly slowed hypotonicity-induced YFP quenching (Fig. 1C). *LRRC8A* knockdown also strongly suppressed $I_{Cl(swell)}$ in patch-clamp experiments (Fig. 1, D to F), suggesting that the multispan membrane protein LRRC8A is an indispensable component of VRAC or is needed for its activation.

Although LRRC8A reached the plasma membrane (Fig. 1G, and fig. S4A for HeLa cells), its transfection into HEK cells rather decreased $I_{Cl(swell)}$

(Fig. 1F). We hypothesized that VRAC contains LRRC8A as part of a heteromer and that LRRC8A overexpression led to a subunit stoichiometry that was incompatible with channel activity. LRRC8A has four closely related homologs (LRRC8B to LRRC8E), which all have four predicted trans-membrane domains (19, 20). Expressed sequence tag (EST) databases suggested that all homologs were widely expressed. Immunocytochemistry of transfected HeLa cells (fig. S4A) and of native HEK cells (Fig. 1, G and H) detected LRRC8A at

the plasma membrane. Truncation of its C terminus, as in a patient with agammaglobulinemia (21), led to cytoplasmic retention (fig. S4B). LRRC8B through LRRC8E remained intracellular when transfected alone, but reached the plasma membrane when cotransfected with LRRC8A (Fig. 1, I and J, and fig. S4, C to H). Unlike LRRC8A transfection, LRRC8A and LRRC8C coexpression did not suppress $I_{Cl(swell)}$ (Fig. 1F). However, neither this coexpression, nor any other combination tested, significantly increased current amplitudes above wild-type (WT) values.

We used zinc-finger nuclease and clustered regularly interspaced short palindromic repeats (CRISPR)-Cas (22) technologies to constitutively disrupt *LRRC8* genes. In addition to polyploid HEK cells, we used stably diploid human HCT116 cells for increased disruption efficiency. Gene disruption was confirmed by sequencing and Western blots (Fig. 2A and table S3). To exclude off-target effects, we generated two HEK and three HCT116 lines in which *LRRC8A* was disrupted at different positions (tables S3 and S4). $I_{Cl(swell)}$ was abolished in all five lines and could be rescued by LRRC8A transfection (Fig. 2, B and C, and fig. S5), demonstrating that LRRC8A is essential for $I_{Cl(swell)}$. We also produced HCT116 cells in which other *LRRC8* genes were disrupted singly or in combinations, including a line with disruption of all five *LRRC8* genes (henceforth called *LRRC8*^{-/-} cells). Except for *LRRC8A*, disruption of single *LRRC8* genes did not abolish VRAC currents (Fig. 2, B and C). However, $I_{Cl(swell)}$ amplitudes were robustly reduced in *LRRC8E*^{-/-} and in *LRRC8(C/E)*^{+/+} double and *LRRC8(C/D/E)*^{+/+} triple knockout (KO) cells. $I_{Cl(swell)}$ was abolished in *LRRC8(B/C/D/E)*^{-/-} cells (Fig. 2, B and C). $I_{Cl(swell)}$ inactivated faster and at less positive potentials in *LRRC8C*^{-/-} and *LRRC8(C/E)*^{-/-} cells compared to WT HCT116, *LRRC8B*^{-/-}, *LRRC8D*^{-/-}, or *LRRC8E*^{-/-} cells. By contrast, $I_{Cl(swell)}$ inactivated more slowly and at more positive voltages in *LRRC8(D/E)*^{-/-} HCT116 cells (Fig. 2, B and D, and fig. S6D) and in WT HEK cells (Figs. 1E and 2D). $I_{Cl(swell)}$ of these mutant cell lines retained the ion selectivity of WT VRAC with the characteristic $\Gamma^- > NO_3^- > Cl^- \gg Glc^-$ (gluconate) permeability sequence (fig. S6A).

LRRC8A transfection into quintuple KO *LRRC8*^{-/-} cells failed to rescue $I_{Cl(swell)}$ (Fig. 2, E and F), agreeing with the absence of $I_{Cl(swell)}$ in *LRRC8(B/C/D/E)*^{-/-} cells (Fig. 2, B and C). Cotransfecting *LRRC8*^{-/-} cells with LRRC8A and either LRRC8C or LRRC8E yielded $I_{Cl(swell)}$ with current densities similar to those of native cells (Fig. 2F). Coexpressing LRRC8A with LRRC8D yielded lower currents (Fig. 2, E and F). No current was observed upon coexpression of LRRC8A and LRRC8B, which may relate to the poor expression of LRRC8B (Fig. 3, D and F). These findings are consistent with the low currents observed in *LRRC8(C/E)*^{-/-} cells (Fig. 2C), where LRRC8A can only interact with poorly expressed LRRC8B and/or LRRC8D. Reconstituted $I_{Cl(swell)}$ activated similarly to WT VRAC

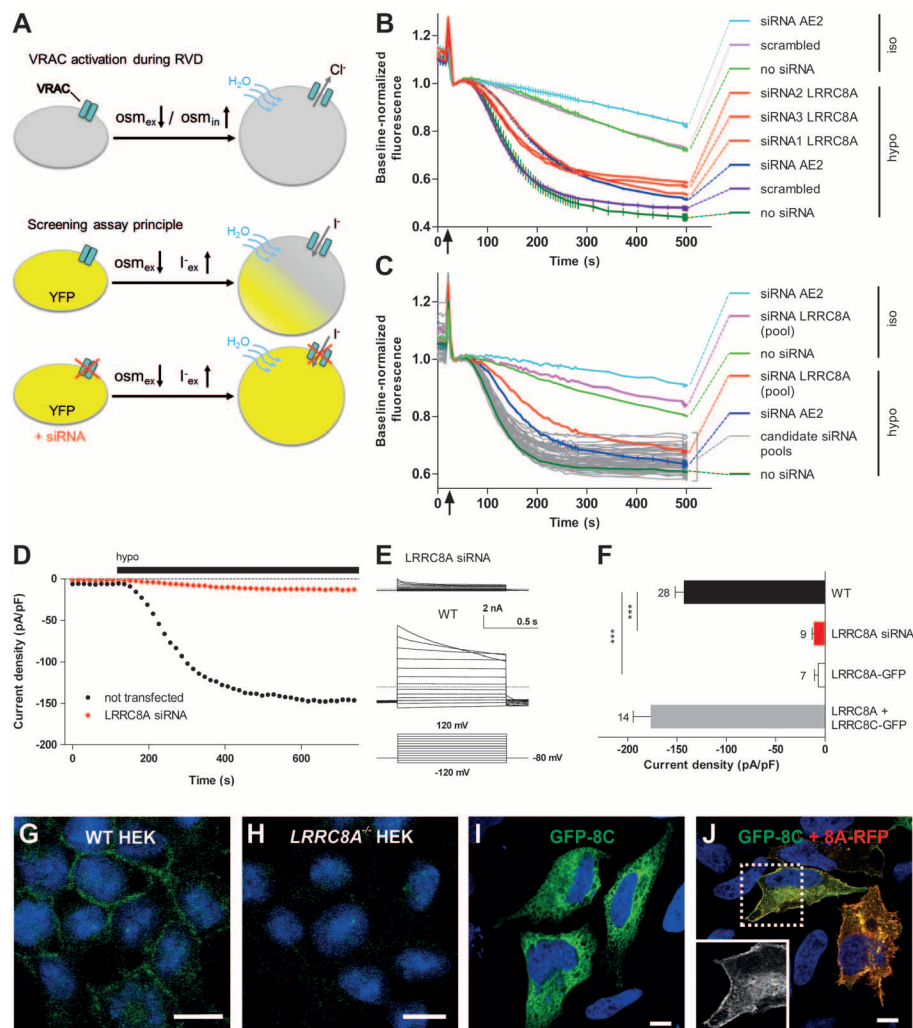


Fig. 1. siRNA screen for volume-regulated anion channel VRAC identifies LRRC8A. (A) Principle of screen. Top: In regulatory volume decrease (RVD), VRAC releases Cl^- . Bottom: Quenching of YFP fluorescence by Γ^- entering through VRAC used as readout. (B) Example traces, normalized to fluorescence at ~30 to 50 s. Traces averaged from wells treated with control siRNAs (scrambled, AE2, both $n = 3$) and no siRNA ($n = 2$) (error bars, SEM), and individual traces from wells singly transfected with the three siRNAs against LRRC8A. Except for LRRC8A siRNA2 and 3, all traces are from the same plate. Arrow indicates addition of Γ^- -containing hypotonic (hypo; 229 mOsm) or isotonic (iso; 329 mOsm) saline. (C) Secondary screen using siRNA pools against candidate genes. Averaged control traces as in (B). (D) Typical time course of VRAC activation in WT or LRRC8A siRNA-treated HEK cells. Current densities at -80 mV are shown. Bar, application of hypotonic (240 mOsm) saline (hypo). (E) Current traces of fully activated $I_{Cl(swell)}$ measured with the protocol shown below. Dotted lines indicate zero current. (F) $I_{Cl(swell)}$ amplitudes (at -80 mV) of WT HEK cells, cells treated with LRRC8A siRNA, or transfected with indicated LRRC8 cDNAs. Error bars, SEM; number of experiments is indicated; $***P < 0.001$. (G) Plasma membrane localization of endogenous LRRC8A in HEK cells. (H) No LRRC8 labeling in *LRRC8A*^{-/-} HEK cells. (I) LRRC8C is intracellular when transfected into HeLa cells, but (J) reaches the plasma membrane when cotransfected with LRRC8A. (Inset) Magnification of boxed area showing only GFP fluorescence. Scale bars, 10 μ m.

upon swelling (Fig. 2E) and displayed its typical anion permeability sequence (fig. S6, B and C).

$I_{Cl(swell)}$ inactivated more slowly and at more positive voltages when LRRC8A was coexpressed with LRRC8C in *LRRC8*^{-/-} cells compared to cells coexpressing LRRC8A with LRRC8E or LRRC8D (Fig. 2, E and G, and fig. S6E). This observation was in agreement with the faster $I_{Cl(swell)}$ inactivation in *LRRC8C*^{-/-} cells (Fig. 2, B and D, and fig. S6D) in which the “decelerating” LRRC8C subunit may be replaced by LRRC8E or other “accelerating” subunits.

Native $I_{Cl(swell)}$ currents display different inactivation kinetics (3). Whereas $I_{Cl(swell)}$ shows

prominent inactivation at positive potentials in HEK cells (23, 24) (Fig. 1E, Fig. 2D, and fig. S6D) and even more inactivation in HCT116 cells (Fig. 2, B and D, and fig. S6D), it inactivates much less in blood cells such as promyelocytic HL-60 cells and in vascular smooth muscle and neurons (24–26). EST databases suggest that these cells express the “decelerating” subunit LRRC8C, but lack LRRC8E that potently induces inactivation (Fig. 2, E and G, and fig. S6E). Quantitative reverse transcription–polymerase chain reaction confirmed that HEK and HCT116 cells expressed LRRC8A through LRRC8E, whereas LRRC8E was almost absent from HL-60 cells (fig. S7).

Moreover, HCT116 cells, whose $I_{Cl(swell)}$ inactivates to a greater extent than that of HEK cells (Fig. 1E, Fig. 2, B and D, and fig. S6D), express less “decelerating” LRRC8C than HEK (fig. S7).

LRRC8 proteins have four predicted transmembrane domains (TMDs) followed by hydrophilic C termini with up to 17 leucine-rich repeats (27) (Fig. 3A). Their C termini were originally thought to be extracellular (19, 21), but proteome databases revealed (20) that the TMD2-TMD3 linker can be phosphorylated and suggested that LRRC8 N and C termini are cytoplasmic (Fig. 3A). LRRC8 proteins display weak homology (20) to pannexins, pore-forming proteins (28) with

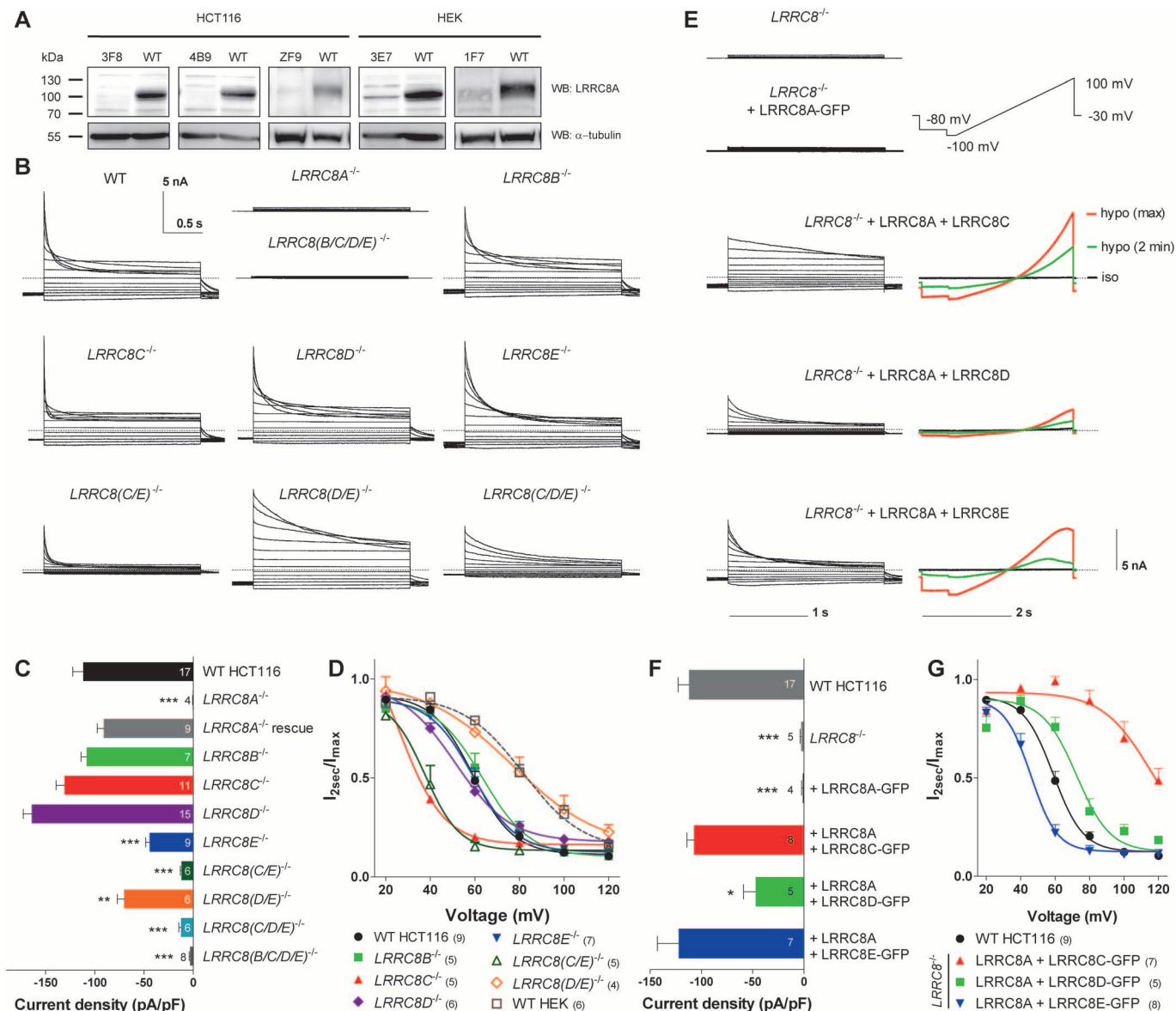


Fig. 2. Characterization of *LRRC8* KO cells and of reconstituted $I_{Cl(swell)}$. (A) Western blots confirm *LRRC8A* disruption in mutant cell lines (table S3). α -Tubulin, loading control. (B) Example $I_{Cl(swell)}$ traces (as in Fig. 1E, but 2-s pulses) of WT and mutant HCT116 cells. (C) Current densities (at -80 mV) of maximally activated $I_{Cl(swell)}$ of WT and mutant HCT116 cells. (D) $I_{Cl(swell)}$ inactivation assessed by ratio of current at end and beginning of pulse. (E) When transfected into HCT116 *LRRC8*^{-/-} cells (with all *LRRC8* genes disrupted),

LRRC8A rescues $I_{Cl(swell)}$ only with LRRC8C, D, or E [left panels; example traces measured as in (B)]. Right panels, example ramp current traces from reconstituted $I_{Cl(swell)}$ at isotonicity (black), 2 min after switching to hypotonicity (green) and with maximal activation (red). Ramp protocol shown at top. (F) $I_{Cl(swell)}$ current densities at -80 mV for indicated combinations. (G) Voltage-dependent inactivation of $I_{Cl(swell)}$. Error bars, SEM. Number of cells is shown in parentheses. **P* < 0.05, ***P* < 0.01, and ****P* < 0.001 versus WT.

connexin-like topology. Connexins form hexameric hemichannels and gap junctions (29). This similarity suggested (20) that LRRC8 proteins form hexameric channels for as yet unknown substrates. Like VRAC currents (14, 15, 30), LRRC8 proteins are found in vertebrates but not in other phyla such as arthropoda (20).

We ascertained the pannexin- and connexin-like transmembrane topology of LRRC8A. Mutating potential N-linked glycosylation sites between TMD1 and TMD2 abolished the size shift upon PNGaseF treatment (Fig. 3B), demonstrating that this loop is extracellular. Immunofluorescence of cells transfected with hemagglutinin (HA)–

tagged LRRC8A constructs showed that the TMD3–4 segment is extracellular and the C terminus cytoplasmic (Fig. 3C).

The formation of LRRC8 heteromers was confirmed by coimmunoprecipitation from HEK cells transfected with LRRC8A and epitope-tagged versions of either LRRC8B, C, D, or E. LRRC8A coprecipitated each of the other isoforms, but not the Cl[−] channel CIC-1 used as a control (Fig. 3, D and E). Conversely, precipitation of epitope-tagged versions of LRRC8B through LRRC8E coprecipitated LRRC8A (Fig. 3F). Coprecipitation of LRRC8 isoforms was also observed for native HEK cells (fig. S8).

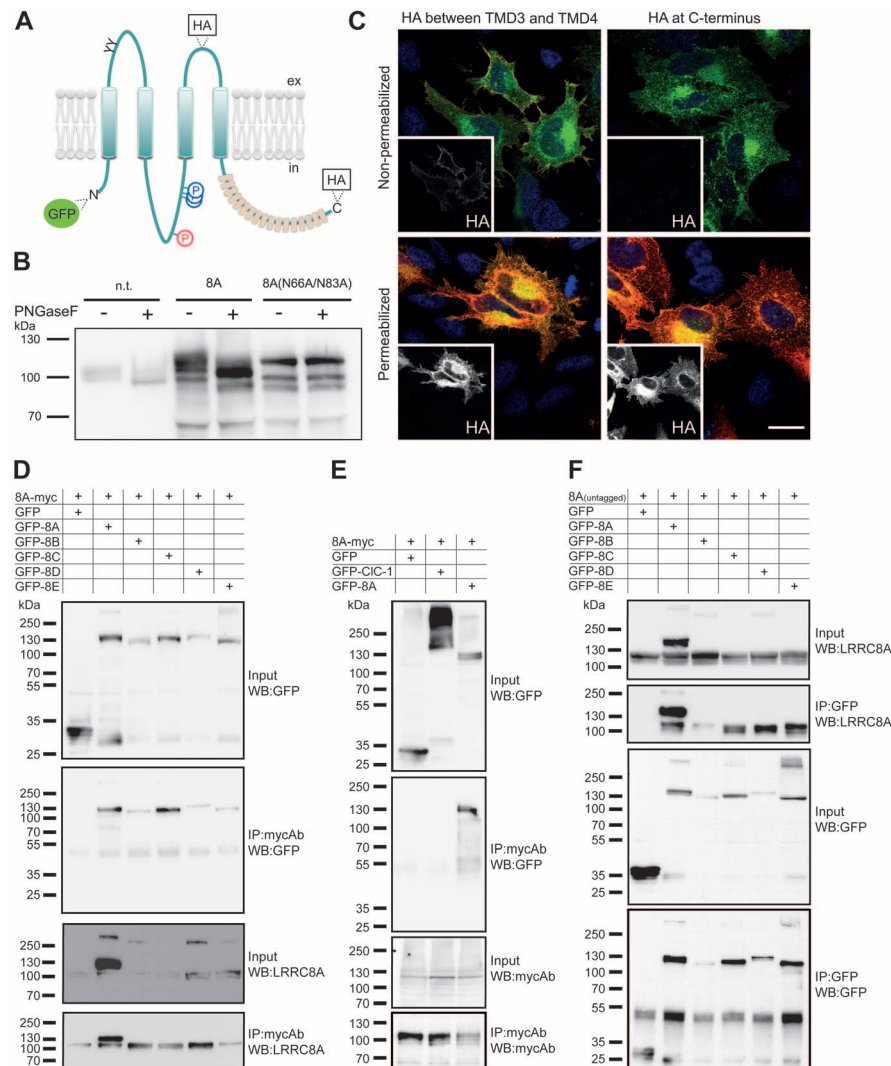


Fig. 3. Transmembrane topology and heteromerization of LRRC8A. (A) LRRC8A model [modified from (20)]. Four transmembrane domains precede a C terminus with up to 17 leucine-rich repeats (27) (orange). Phosphoserines in LRRC8A (red P) and LRRC8D (blue P), according to Uniprot (32), predicted N-linked glycosylation sites (Y), and added epitopes are indicated. (B) PNGaseF treatment of endogenous LRRC8A, transfected LRRC8A, but not of LRRC8A(N66A,N83A) with disrupted glycosylation sites, decreased LRRC8A size in Western blots. The changed banding pattern of LRRC8A(N66A,N83A) suggests altered posttranslational modifications. n.t., nontransfected. (C) Immunofluorescence of nonpermeabilized and permeabilized HeLa cells transfected with HA-tagged GFP-LRRC8A. Overlays of GFP (green) and HA (red) labeling. Insets show exclusively HA staining. Scale bar, 20 μ m. (D) LRRC8A coprecipitated epitope-tagged LRRC8B through LRRC8E in double-transfected HEK cells. LRRC8B and LRRC8D were poorly expressed. (E) LRRC8A did not coprecipitate the CIC-1 Cl[−] channel. (F) Epitope-tagged LRRC8B through LRRC8E coprecipitated LRRC8A.

Hypotonicity induced a robust taurine efflux from HEK and HCT116 cell lines, but not from their *LRRC8A*^{−/−} derivatives (Fig. 4A and fig. S9A), where taurine efflux could be rescued by LRRC8A and LRRC8C cotransfection (fig. S9B for HEK cells). Taurine efflux was also abolished in *LRRC8(B/C/D/E)*^{−/−} HCT116 cells (Fig. 4A). Because both *I*_{Cl(swell)} and swelling-induced taurine efflux similarly depended on LRRC8 heteromers, VRAC is most likely identical to VSOAC, the volume-sensitive organic osmolyte/anion channel (7). Accordingly, *LRRC8A*^{−/−} HEK cells showed severely impaired volume regulation. After initial swelling, WT, but not *LRRC8A*^{−/−}, cells slowly reduced their volume in the continuous presence of extracellular hypotonicity (Fig. 4B). Hence, LRRC8-containing VSOAC plays a major role in RVD.

The absence of *I*_{Cl(swell)} upon genomic disruption of *LRRC8A* and its rescue by transient reexpression identified LRRC8A as an indispensable component of VRAC, or alternatively, as being crucial for its activation. The wide expression pattern of *LRRC8* genes and the plasma membrane residency of LRRC8A-containing heteromers fulfill the prerequisites for LRRC8 proteins forming the channel. The dependence of current properties on LRRC8 isoform combinations indicated that LRRC8 heteromers are integral components

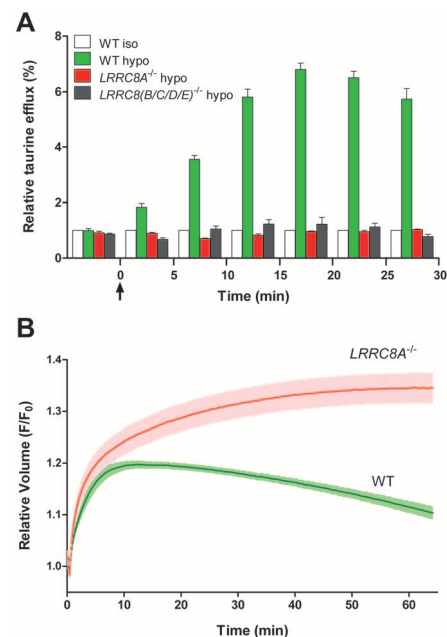


Fig. 4. LRRC8 proteins are crucial for swelling-induced taurine efflux and RVD. (A) ³[H]-Taurine efflux from HCT116 cells of indicated genotypes. Cells were either in isotonic solution throughout (WT, white bars) or exposed to hypotonic solution starting at *t* = 0 (arrows). Bars, means of six measurements; error bars, SEM. (B) WT and *LRRC8A*^{−/−} HEK cells were shifted to hypotonic saline (96 mOsm) at *t* = 30s, and cell volume was monitored by calcein fluorescence. Mean of six measurements; error range, SEM. Similar results were obtained in three experiments.

of VRAC, a notion buttressed by the homology of LRRC8 proteins to pannexins. Because cotransfection of LRRC8 isoforms did not significantly increase $I_{Cl(swell)}$ amplitude over that of the WT, other factors limit VRAC activity; for example, an auxiliary subunit of VRAC or part of the signaling cascade leading to its activation. Indeed, VRAC currents seem to be highly regulated, with amplitudes differing by a factor of only 2 to 3 across cell types (3, 30).

The homology between LRRC8 proteins and pannexins suggested that LRRC8 proteins form hexameric channels (20). We confirmed the pannexin-like topology of LRRC8A and propose that VRAC is formed by LRRC8 hexamers of LRRC8A and at least one other family member. In this model, VRAC may contain two to five different LRRC8 isoforms, creating a potentially large variety of VRAC channels with different properties. The variation of $I_{Cl(swell)}$ inactivation kinetics between different tissues and cells (3) can be ascribed to different expression ratios of LRRC8 isoforms. LRRC8-dependent Cl^- and taurine fluxes indicated that VRAC is identical to VSOAC (6) and fit to a pore formed by LRRC8 hexamers, because hexameric pannexin channels likewise display poor substrate specificity (28).

Our results provide the basis to explore the structure-function relationship of VRAC/VSOAC, to clarify the signaling pathway that couples cell volume increase to channel opening, and to investigate the role of the channel in basic cellular processes such as cell division, growth, and mi-

gration and in various pathological states. Interestingly, a truncating *LRRC8A* mutation has been described in a patient with agammaglobulinemia (21), and *LRRC8C* may have a role in fat metabolism (31).

References and Notes

- E. K. Hoffmann, I. H. Lambert, S. F. Pedersen, *Physiol. Rev.* **89**, 193–277 (2009).
- H. Pasantes-Morales, R. A. Lezama, G. Ramos-Mandujano, K. L. Tuz, *Am. J. Med.* **119** (suppl. 1), S4–S11 (2006).
- B. Nilius *et al.*, *Prog. Biophys. Mol. Biol.* **68**, 69–119 (1997).
- Y. Okada, K. Sato, T. Numata, *J. Physiol.* **587**, 2141–2149 (2009).
- Y. Okada, *Am. J. Physiol.* **273**, C755–C789 (1997).
- P. S. Jackson, K. Strange, *Am. J. Physiol.* **265**, C1489–C1500 (1993).
- K. Strange, P. S. Jackson, *Kidney Int.* **48**, 994–1003 (1995).
- I. H. Lambert, E. K. Hoffmann, *J. Membr. Biol.* **142**, 289–298 (1994).
- D. B. Shennan, *Cell. Physiol. Biochem.* **21**, 15–28 (2008).
- A. Stutzin *et al.*, *Am. J. Physiol.* **277**, C392–C402 (1999).
- T. Moser, R. H. Chow, E. Neher, *Pflügers Arch.* **431**, 196–203 (1995).
- Y. Okada *et al.*, *J. Membr. Biol.* **209**, 21–29 (2006).
- S. Gründer, A. Thiemann, M. Pusch, T. J. Jentsch, *Nature* **360**, 759–762 (1992).
- S. C. Stotz, D. E. Clapham, *PLOS ONE* **7**, e46865 (2012).
- L. T. Chien, H. C. Hartzell, *J. Gen. Physiol.* **132**, 537–546 (2008).
- R. Fischmeister, H. C. Hartzell, *J. Physiol.* **562**, 477–491 (2005).
- L. J. Galiotta, P. M. Haggie, A. S. Verkman, *FEBS Lett.* **499**, 220–224 (2001).
- V. Benfenati *et al.*, *Channels* **3**, 323–336 (2009).
- K. Kubota *et al.*, *FEBS Lett.* **564**, 147–152 (2004).

- F. Abascal, R. Zardoya, *Bioessays* **34**, 551–560 (2012).
- A. Sawada *et al.*, *J. Clin. Invest.* **112**, 1707–1713 (2003).
- L. Cong *et al.*, *Science* **339**, 819–823 (2013).
- B. Nilius, J. Prenen, U. Wissenbach, M. Bödding, G. Droogmans, *Pflügers Arch.* **443**, 227–233 (2001).
- C. Y. Hernández-Carballo, J. A. De Santiago-Castillo, T. Rosales-Saavedra, P. Pérez-Cornejo, J. Arreola, *Pflügers Arch.* **460**, 633–644 (2010).
- G. X. Wang *et al.*, *Am. J. Physiol. Heart Circ. Physiol.* **287**, H533–H544 (2004).
- J. L. Leaney, S. J. Marsh, D. A. Brown, *J. Physiol.* **501**, 555–564 (1997).
- G. Smits, A. V. Kajava, *Mol. Immunol.* **41**, 561–562 (2004).
- S. Penuela, R. Gehi, D. W. Laird, *Biochim. Biophys. Acta* **1828**, 15–22 (2013).
- S. Maeda *et al.*, *Nature* **458**, 597–602 (2009).
- B. Nilius *et al.*, *Pflügers Arch.* **428**, 364–371 (1994).
- T. Hayashi *et al.*, *Biol. Pharm. Bull.* **34**, 1257–1263 (2011).
- M. Magrane, U. Consortium, *Database (Oxford)* **2011**, bar009 (2011).

Acknowledgments: We thank M. Neuenschwander for technical advice concerning the assay; H.-P. Rahn for help with fluorescence-activated cell sorting; A. Brockhoff and W. Meyerhof for use of their Fluorometric Image Plate Reader in a pilot experiment; and J. Liebold, N. Krönke, J. Jedamzick, and S. Kleistle for technical assistance. Supported by the European Research Council Advanced Grant (FP/2007-2013) 294435 “Cytovolution” and the Deutsche Forschungsgemeinschaft (Exc 257 “Neurocure”) to T.J.J.

Supplementary Materials

www.sciencemag.org/content/344/6184/634/suppl/DC1

Materials and Methods

Author Contributions

Figs. S1 to S10

Tables S1 to S4

References (33–38)

3 March 2014; accepted 2 April 2014

Published online 10 April 2014;

10.1126/science.1252826

Gibberellin Acts Positively Then Negatively to Control Onset of Flower Formation in *Arabidopsis*

Nobutoshi Yamaguchi,¹ Cara M. Winter,^{1*} Miin-Feng Wu,¹ Yuri Kanno,² Ayako Yamaguchi,¹ Mitsunori Seo,² Doris Wagner^{1†}

The switch to reproductive development is biphasic in many plants, a feature important for optimal pollination and yield. We show that dual opposite roles of the phytohormone gibberellin underpin this phenomenon in *Arabidopsis*. Although gibberellin promotes termination of vegetative development, it inhibits flower formation. To overcome this effect, the transcription factor LEAFY induces expression of a gibberellin catabolism gene; consequently, increased LEAFY activity causes reduced gibberellin levels. This allows accumulation of gibberellin-sensitive DELLA proteins. The DELLA proteins are recruited by SQUAMOSA PROMOTER BINDING PROTEIN-LIKE transcription factors to regulatory regions of the floral commitment gene *APETALA1* and promote *APETALA1* up-regulation and floral fate synergistically with LEAFY. The two opposing functions of gibberellin may facilitate evolutionary and environmental modulation of plant inflorescence architecture.

Synchronization of the developmental transitions that lead to reproductive competence is important for species survival. Plants form new lateral organs iteratively throughout their life from the flanks of the shoot apical meristem (fig. S1) (1, 2). The type of the

lateral organ produced depends on the phase of the life cycle. In *Arabidopsis*, rosette leaves are produced during the vegetative phase. During the reproductive phase, an inflorescence forms. Not all lateral organ primordia of the inflorescence are competent to become flow-

ers. Those that are not instead give rise to branches subtended by cauline leaves during the first inflorescence phase (3, 4). The duration of the branch-producing first inflorescence phase determines inflorescence architecture and is critical for optimal seed set.

To gain insight into the regulation of the transition from branch to floral fate in the lateral primordia of the inflorescence, we analyzed public genome-wide binding and expression data and identified genes that are direct targets of the LEAFY (LFY) transcription factor (5–7) (table S1). LFY promotes flower formation (8, 9). We identified for further study the *EUI-LIKE P450 A1* (*ELAI*) gene (fig. S2), which encodes a cytochrome P450 (10). *ELAI* expression was very low in vegetative tissues but increased when flowers formed (fig. S3). On the basis of in situ hybridization and reporter studies, *ELAI* was initially expressed on the abaxial side of incipient flower primordia and later along their entire circumference (Fig. 1A and fig. S3). *ELAI* expression was dependent on the

¹Department of Biology, University of Pennsylvania, 415 South University Avenue, Philadelphia, PA 19104–6018, USA. ²RIKEN Center for Sustainable Resource Science, Yokohama, Kanagawa, 230-0045, Japan.

*Present address: Department of Biology, Duke University, Box 90338, Durham, NC 27708, USA.

†Corresponding author. E-mail: wagnerdo@sas.upenn.edu



Supplementary Materials for
**Identification of LRRC8 Heteromers as an Essential Component of the
Volume-Regulated Anion Channel VRAC**

Felizia K. Voss, Florian Ullrich, Jonas Münch, Katina Lazarow, Darius Lutter, Nancy Mah, Miguel A. Andrade-Navarro, Jens P. von Kries, Tobias Stauber,* Thomas J. Jentsch*

*Corresponding author. E-mail: jentsch@fmp-berlin.de (T.J.J.); tstauber@fmp-berlin.de (T.S.)

Published 10 April 2014 on *Science Express*
DOI: 10.1126/science.1252826

This PDF file includes:

Materials and Methods
Author contributions
Figs. S1 to S10
Tables S1 to S4
References

Supplementary Materials:

Materials and Methods

Author contributions

Figures S1-S10

Tables S1-S4

References 33-38

Materials and Methods

HEK293-YFP Cell Line Used in the siRNA Screen

The T-REx® system (Life Technologies) was used to generate a stable HEK293 cell line inducibly expressing the halide-sensitive YFP(H148Q/I152L) (17). Clones were selected using 200 µg/ml hygromycin B and 10 µg/ml blasticidin. Monoclonal cell lines were subsequently tested for robust and homogenous expression of YFP after induction with 1.25 µg/ml doxycycline using life-cell imaging. The clone 1:5-(6) was chosen for the genome-wide screening procedure. The cells were kept in DMEM with tetracycline-free Hyclone FCS (Thermo Scientific) and the above-mentioned antibiotics.

Genome-wide siRNA Screen

The screen was performed at the FMP Screening Unit using the Ambion Silencer® Human Genome siRNA Library V3 (Life Technologies) containing 189 384-well plates. This library targets each gene by three independently placed siRNAs. The screen was performed in two replicates. Each screening plate contained several controls like siRNA pools against YFP (Silencer GFP siRNA from Ambion), a non-targeting siRNA (Silencer Negative Control from Ambion), an siRNA pool against AE2 (ON-TARGETplus SMARTpool siRNA SLC4A2 from Thermo Scientific) and a cell death-inducing siRNA mixture (AllStars Hs Cell Death Control siRNA from Qiagen). For detailed plate layout see fig. S2. For siRNA transfection, in each well of the 384-well assay-plate 8 µl of a 500 nM library-siRNA-OptiMEM® solution was mixed with 0.2 µl Lipofectamine® RNAimax transfection reagent (Life Technologies) previously diluted in 11.8 µl Opti-MEM® (Life Technologies). Subsequently 6000 cells/well in antibiotic-free DMEM were seeded onto the pre-dispensed transfection mixture using a BioTek EL406™ dispenser resulting in a final concentration of 50 nM siRNA in a total volume of 80 µl per well. After 24 h the cell culture medium was exchanged to phenol red-free DMEM containing 1.25 µg/ml doxycycline to induce YFP-expression.

The YFP-quenching assay was performed 72 h post-transfection. After having exchanged the cell culture medium in all wells of the plate with 10 µl of isotonic solution (in mM: 145 NaCl, 5 KCl, 1 MgCl₂, 2 CaCl₂, 10 glucose, 10 HEPES pH 7.4, 329 mOsm) in a

Tecan Freedom EVO 200 workstation, the plates were transferred into the FLIPR™ (Molecular Devices) High Throughput Cellular Screening Device and fluorescence measurements were initiated. All wells of the plate were simultaneously illuminated at $\lambda = 495\text{-}505\text{ nm}$ and YFP-fluorescence was measured at $\lambda = 526\text{-}585\text{ nm}$ using the FLIPR Fluo3 LED/filter set. After 5 measurements in intervals of 5 s, parallel pipetting within the FLIPR™ added 25 μl iodide-containing hypotonic (rows 1-23) (in mM: 70 NaI, 5 NaCl, 5 KCl; 1 MgCl_2 , 2 CaCl_2 , 10 glucose, 10 HEPES pH 7.4, 189 mOsm) or isotonic (row 24) (in mM: 70 NaI, 5 NaCl, 5 KCl; 1 MgCl_2 , 2 CaCl_2 , 10 glucose, 140 mannitol, 10 HEPES pH 7.4, 329 mOsm) solution into each well. The solution added to wells O23, P23, O24 and P24 was hypotonic and contained 1% Triton X100. The mixture of the pre-existing 10 μl isotonic solution and the newly added 25 μl hypotonic solution resulted in a final osmolarity of 229 mOsm, i.e. a ~30% decrease in osmolarity, and a final concentration of 50 mM iodide. Fluorescence measurements were continued for 55 s in 5-s intervals, followed by 8 measurements in 30-s intervals to minimize bleaching, and finally 10 measurements in 1-s intervals. The total amount of measurement (500 s) was sufficient for YFP-quenching to nearly reach steady state. At time points 0 s and 5 s (before pipetting) and at 25, 30, 35, 40, 45, and 490 s (during/after pipetting) photographs of the entire plate were taken to allow post-hoc control of the integrity of the cell layers of each well. All original fluorescence traces were stored for re-analysis.

Parameters Extracted from FLIPR™ Screen and Bioinformatics Analysis

Several parameters were extracted from the primary data and used for subsequent data evaluation (fig. S3, A and B). The averaged fluorescence before the pipetting step, $F_{\text{ante}}^{\text{abs}}$, was obtained by averaging values from measurements 1-3 and was used to set a warning 'low cell' flag when its value was less than 0.8 times of mean $F_{\text{ante}}^{\text{abs}}$ averaged over all experimental wells from the plate. After pipetting, the fluorescence acutely changed to new values that were more or less stable for about 30 s before swelling-induced quenching of YFP set in. We averaged fluorescence values from measurements 9 to 12 to obtain $F_{\text{start}}^{\text{abs}}$ which was subsequently used for normalization. $F_{\text{fin}}^{\text{abs}}$ was defined as averaged fluorescence from the four last measurements and we set another warning flag if fluorescence had not reached quasi-steady-state at the end of the measurement. $F_{\text{fin}}^{\text{abs}}$ might be used for background subtraction. We preferred, however, to subtract $F_{\text{BG TX100}}$, the averaged (over the last 300 s) fluorescence of the four control wells from the same plate that had been exposed to Triton X100 to maximally quench YFP fluorescence. The background-subtracted fluorescence value of each well was then normalized to the corresponding $F_{\text{start}}^{\text{abs}}$ value to yield F^* (fig. S3B).

siRNA-mediated knock-down of VRAC should reduce iodide current magnitude, but not necessarily the final intracellular iodide concentration (reflected in $F_{\text{fin}}^{\text{abs}}$). Although not

being a linear function of iodide influx, the speed of YFP quenching after exposure to hypotonicity is the best indicator for the magnitude of VRAC currents. We therefore determined the slope of fluorescence change by linear regression of 11 points in a sliding window between 35 and 350 s. The maximum of these slopes was defined as S_{\max} . The intersection of the corresponding linear regression line with $F^*=1$ defined t_{onset} as a measure for the speed of response to the hypotonic challenge, a delay that might be changed e.g. by interfering with the signal transduction cascade leading to VRAC opening (fig. S3B). For each individual plate we then calculated the mean maximal slope S_{\max}^{mean} of all experimental wells and the corresponding standard deviation. S_{\max} of each individual siRNA-treated well was expressed in terms of standard deviations to yield Z-scores, with e.g. $Z=2$ meaning that the slope is slower by two standard deviations compared to the average of the plate.

siRNAs leading to cell death or targeting YFP confirmed that results of none of the 384-well plates had to be discarded because of low transfection efficiency. Results were sorted by genes and listed individually for each of the three siRNAs (which generally were on different plates) the Z-score, t_{onset} , $F_{\text{ante}}^{\text{abs}}$, $F_{\text{fin}}^{\text{abs}}$, the low-cell and the non-steady-state flags (1 or 0). It also listed the protein families associated with the gene products (as obtained from UniProtKB database (32)), the genes' tissue expression pattern (as determined by publicly available microarray data (33)) and predicted number of transmembrane domains that was calculated by the software TMHMM 2.0c (34). Comparison of the first and replicate screen showed that the effects of individual siRNAs on the respective Z-scores of S_{\max} correlated reasonably well and demonstrated the usefulness of our warning flags (fig. S3, C and D). To account for different efficiencies of siRNA knock-down with the three individual siRNAs against each gene, some of which may be ineffective or show off-target effects, we sorted our results according to the mean Z obtained with the two 'best' siRNAs (giving the largest values of Z).

As expected, many of the hits could be ruled out by one or more criteria. For instance, siRNAs against several ribosomal proteins led to large Z-scores that were caused by poor cell growth or cell death as indicated by the 'low cell' flag. Large Z-scores that were not reproduced in the replicate screen could sometimes be eliminated by examining the photographs of the plates which showed dirt at the respective well that had caused high background fluorescence. As we were looking for the channel itself and not for proteins involved in the activation of VRAC, we limited our search to proteins having at least one predicted transmembrane domain. Many candidates could be eliminated by their well-established function or their inclusion in well-known gene families like olfactory receptors or other G-protein coupled receptors. However, as annotations are not always reliable and as proteins may serve more than one function, several candidates whose annotated function appeared to be incompatible with VRAC function but which otherwise seemed promising

were earmarked for a secondary screen. As VRAC currents have been observed in every mammalian tissue that has been investigated, we excluded candidates that showed a narrow tissue distribution or very low expression levels as indicated by NCBI EST profile databases or the scientific literature, except when they belonged to a gene family whose overlapping expression pattern covered many tissues.

On the basis of these criteria 87 candidate genes (table S2) were selected for a secondary screen that used again the FLIPR™ assay with pools of four siRNAs (ON-TARGETplus SMARTpool siRNA, Thermo Scientific) that were different from the ones used in the primary screen. Of these genes, only *LRRC8A* passed the test. The SMART pool directed against *LRRC8A* slowed hypotonicity-induced quenching of YFP fluorescence better than the SMART-pool against *AE2* (Fig. 1C). It is interesting to note that *LRRC8A* was at the 222nd position of hits sorted exclusively by the mean Z-score averaged across both screens from the 2 out of 3 siRNAs per gene that gave the best score. Only one of the three siRNAs against *LRRC8A* gave a Z-score for maximal slope of ~2, the two others were below 1 (fig. S3E).

Generation of Monoclonal Knock-out Cell Lines Using the CRISPR/Cas and Zinc-finger Nuclease Technologies

For the disruption of *LRRC8* genes by the CRISPR/Cas system in cell culture, we used the px330 single plasmid system as described (22). The targeting sgRNA sequences were chosen using both the UCSC Genome Browser tool at www.genome-engineering.org and the sequence collection from (35) (for sequences, table S4). Target sgRNAs were cloned into the px330 vector and transfected into the described YFP expressing HEK293 clone or WT HCT116 cells in a 6-well format using 3 µl of the Fugene HD transfection reagent and 900 ng targeting vector(s) (up to 4) plus 100 ng pEGFP-C1-vector. In HCT116 cells, the *LRRC8A* gene was additionally disrupted using custom-designed CompoZr® Knock-out Zinc-Finger Nucleases (Sigma). The zinc-finger nuclease (ZFN) pair encoded on two separate plasmids was transfected as the CRISPR/Cas constructs described above, using 500 ng of each ZFN-plasmid and 100 ng of the pEGFP-C1 vector. 2-5 days post-transfection single GFP-positive cells were FACS-sorted into 96-well plates containing preconditioned DMEM (for HEK cells) or McCoy's 5A (for HCT116 cells) medium. In some cases, transfected cells were enriched by G418 selection before FACS sorting.

Monoclonal cell lines were raised and tested for sequence alterations using target-site-specific PCR on genomic DNA followed by Sanger-sequencing and/or Western blot analysis to confirm the absence of the protein when specific antibodies were available. To generate multiple KOs of several genes, the respective plasmids were transfected together, or cell lines already carrying *LRRC8* gene disruptions were targeted again for other *LRRC8* genes.

Antibodies

Polyclonal antibodies against LRRC8A were raised in rabbits against the peptide QRTKSRIEQGIVDRSE that was coupled to KLH through an N-terminally added cysteine. Its sequence corresponds to LRRC8A protein sequence between TMD2 and TMD3. Polyclonal antibodies against the C-terminus of LRRC8E were raised in rabbits against the peptide LYEGLPAEVREKMEEEE that was also coupled with an N-terminally added cysteine to KLH. Sera were affinity-purified against the respective peptide and proved specific in Western blots (Fig. 2A and fig. S10, A and B) and—for LRRC8A—in immunofluorescence (Fig. 1, G and H, and fig. S10C). The rabbit anti-KCC1 antibody was described previously (36).

The following commercial primary antibodies were used: rabbit anti-myc (A-14, Santa Cruz Biotechnology), rabbit anti-GFP (A-11122, Life Technologies) for IP and chicken anti-GFP (1020, Aves Lab) for Western blot, mouse anti- α -tubulin (DM1A, Sigma), mouse anti-HA (HA.11, Covance). Secondary antibodies were conjugated to AlexaFluor 488 or 546 (Molecular Probes) or to horseradish peroxidase (Jackson ImmunoResearch).

Expression Constructs and Immunocytochemistry

For expression of LRRC8A - E with GFP fused to their N-termini or C-termini, cDNA encoding the respective human protein (or only aa 1-719 for LRRC8A_{trunc}) was cloned with stop codon into pEGFP-C1 or without stop codon into pEGFP-N1, respectively. For expression of C-terminally RFP-tagged LRRC8A, the cDNA was cloned into pmRFP-N1. cDNA encoding human CIC-1 was in pEGFP-C1. For untagged (co-expression in electrophysiological experiments and LRRC8A antibody testing by Western blot) and C-terminally myc-tagged (deglycosylation experiment and co-immunoprecipitations upon heterologous expression) expression, cDNA encoding LRRC8A was cloned (with and without stop codon, respectively) into pcDNA3.1/myc-His(-)B (Invitrogen). HA-tags (at T307 or at the extreme C-terminus of LRRC8A) and point mutations were introduced by PCR. All constructs were confirmed by sequencing the complete ORF.

For immunocytochemistry, cells were transfected (if indicated) with plasmid encoding the respective construct(s) using Fugene HD. 24-36 h after transfection, cells were fixed in pre-cooled methanol at -20°C for 10 min (immunostaining with LRRC8A antibody), or in 2% (topology assay) or 4% PFA in PBS for 15 min followed by a 5-min incubation with 30 mM glycine in PBS at room temperature. Cells were incubated sequentially for 1 h each with primary and secondary antibodies (where applicable) in PBS containing 0.1% Triton X-100 (or without Triton X-100, for non-permeabilized cells) supplemented with 3% BSA. Images were acquired with an LSM510 confocal microscope with a 63x, 1.4 NA oil-immersion lens (Zeiss).

Quantitative RT-PCR

Total RNA was isolated from cell pellets using the RNeasy Mini Kit (Qiagen). We subjected ~1 µg of RNA to DNase I (amplification grade, Invitrogen) digestion and subsequently transcribed it into cDNA using random primers and Superscript II reverse transcriptase (Invitrogen). A 20-µl qRT-PCR reaction was set up using the Power SYBR Green PCR Master Mix (Applied Biosystems) and 0.5 µM of specific primers. Reactions were run in triplicates with a 60-s elongation time at 60°C. Amplification and melting curves were monitored using a StepOnePlus Real-Time PCR System and StepOne Software (Applied Biosystems). GAPDH was used as internal control and for $\Delta\Delta C_t$ calculations. Primers were designed using the QuantPrime selection tool (37) to preferentially span exon-exon boundaries and to give products of 60–150 bp. The following primer pairs were used (5'-3'):

GAPDH: ACAGTCAGCCGCATCTTCTT and GTTAAAAGCAGCCCTGGTGA
 LRRC8A: GGGTTGAACCATGATTCCGGTGAC and GAAGACGGCAATCATCAGCATGAC
 LRRC8B: ACCTGGATGGCCCACAGGTAATAG and ATGCTGGTCAACTGGAACCTCTGC
 LRRC8C: ACAAGCCATGAGCAGCGAC and GGAATCATGTTTCTCCGGGC
 LRRC8D: ATGGAGGAGTGAAGTCTCCTGTCTG and CTTCCGCAAGGGTAAACATTCTCTG
 LRRC8E: ACCGTGGCCATGCTCATGATTG and ATCTTGCTCCTGTGTACCTGGAG

Electrophysiology

HEK or HCT cells were plated onto gelatine-coated coverslips and transfected using Fugene HD (Promega) or Lipofectamine 2000 (Life Technologies) transfection reagents, respectively. One of the transfected LRRC8 isoforms was fused C-terminally to GFP. When LRRC8A was co-transfected with other LRRC8 isoforms only the latter carried GFP because plasma membrane fluorescence indicated co-expression with LRRC8A.

Whole-cell voltage-clamp experiments were performed in isotonic extracellular solution containing (in mM) 150 NaCl, 6 KCl, 1 MgCl₂, 1.5 CaCl₂, 10 glucose, and 10 HEPES, pH 7.4 with NaOH (320 mOsm). $I_{Cl(swell)}$ was elicited by perfusing the cells with hypotonic solution containing (in mM) 105 NaCl, 6 CsCl, 1 MgCl₂, 1.5 CaCl₂, 10 glucose, 10 HEPES, pH 7.4 with NaOH (240 mOsm). For anion selectivity experiments, NaCl was replaced in this solution by an equimolar amount of NaI, NaNO₃, or Na-D-gluconate. The pipette solution contained (in mM) 40 CsCl, 100 Cs-methanesulfonate, 1 MgCl₂, 1.9 CaCl₂, 5 EGTA, 4 Na₂ATP, and 10 HEPES, pH 7.2 with CsOH (290 mOsm). Osmolarities of all solutions were assessed with an Osmomat 030 freezing point osmometer (Gonotec). All experiments were performed at constant temperature of 20–22°C. Currents were recorded with an EPC-10 USB patch-clamp amplifier and PatchMaster software (HEKA Elektronik) or a MultiClamp 700B patch-clamp amplifier/Digidata 1440A digitizer and pClamp 10 software (Molecular Devices). Patch pipettes had a resistance of 1–3 MΩ. Series resistance was compensated by 80–90% to minimize voltage errors. Currents were sampled at 5 kHz and low-pass filtered at

10 kHz. The holding potential was -30 mV. Cells with a membrane resistance below 800 MΩ or series resistance above 10 MΩ were discarded. The standard protocol for measuring the time course of $I_{Cl(swell)}$ activation, applied every 15 s after membrane rupture, consisted of a 0.6-s step to -80 mV followed by a 2.6-s ramp from -100 to 100 mV. The read-out for $I_{Cl(swell)}$ was the steady-state whole-cell current at -80 mV normalized to the cell capacitance (current density) subtracted by the baseline current density at -80 mV before perfusion with hypotonic solution. The voltage protocol, applied after complete activation of $I_{Cl(swell)}$, consisted of 1-s or 2-s steps starting from -120 mV to 120 mV in 20-mV intervals preceded and followed by a 0.5-s step to -80 mV every 5 s.

Relative anion permeabilities (P_X/P_{Cl}) were calculated from the shifts in reversal potential induced by perfusion with the anion substituted hypotonic salines using a modified Goldman-Hodgkin-Katz equation:

$$P_X / P_{Cl} = \frac{[Cl]_{hypo} \exp\left(-\frac{\Delta E_{rev} F}{RT}\right) - [Cl]_{subst}}{[X]_{subst}}$$

where ΔE_{rev} is the shift in reversal potential, $[Cl]_{hypo}$ and $[Cl]_{subst}$ are the extracellular chloride concentrations in the normal and anion substituted hypotonic saline, and $[X]_{subst}$ is the concentration of the substituting anion. R is the gas constant, T is the absolute temperature, and F is the Faraday constant. Reversal potentials were determined by measuring 3 to 6 cells for each cell line or transfection. Liquid junction potentials were measured for all solutions and corrected for in ion selectivity experiments.

The inactivation kinetics of $I_{Cl(swell)}$ could not be fitted appropriately by a single-exponential function. We therefore calculated the fraction of remaining current by dividing the current amplitude at the end of the 2-s voltage step by the current amplitude 1.5 ms after the beginning of the voltage step (avoiding contamination by capacitive transients). The half inactivation time $t_{1/2}$ was determined by the time point where the inactivation reached half of the total inactivation after 2 s. Calculation of current densities and inactivation characteristics was carried out with an automatic script written in MATLAB R2011a (MathWorks) and plotted with GraphPad Prism 5 (GraphPad Software). Boltzmann curve-fitting and calculation of $V_{1/2}$ was done with GraphPad Prism with the following fitting constraints: bottom value less than 0.2, top value greater than 0.9. Example current traces were lowpass-filtered at 2 kHz and reduced to a sampling rate of 1 kHz for clarity. Averaged data is presented as mean \pm SEM. Significance was calculated by one-way ANOVA and Tukey's post-hoc test, where applicable. At least 4 cells per condition were measured on at least two different days; exact n-values are given in the figures. Where possible, measurements were done blinded.

Deglycosylation, Co-immunoprecipitation and Western Blot

To assess glycosylation of LRRC8A, HEK cells were transfected on 10-cm dishes using 17 μ l of polyethylenimine (PEI) and 6 μ g of plasmid encoding myc-tagged LRRC8A (wild-type or mutant). Cells were lysed in RIPA lysis buffer (150 mM NaCl, 1% NP-40, 0.5% sodium deoxycholate, 0.1% SDS, 50 mM Tris, pH 8.0, 4 mM Pefabloc (Roth), complete proteinase inhibitor cocktail (Roche)). After 10 min centrifugation at 14,000 rpm at 4°C, protein concentrations of cell lysates were determined by BCA assay. 60 μ g of total protein were mixed with 2 μ l of denaturing buffer (NEB) and 2 μ l of 0.1 M Tris/HCl pH 7.4 in a reaction volume of 20 μ l and denatured at 75°C for 10 min. Then 4 μ l of 10xG7 Buffer (NEB), 4 μ l of 10% NP-40 (NEB) and 4 μ l of PNGase F (Roche) were added in a total volume of 40 μ l. After 2 h incubation at 37°C, the reaction was terminated by adding 10 μ l 5xLämmli sample buffer. Samples were separated by SDS-PAGE and analyzed by Western blot using the LRRC8A antibody. The experiment was repeated 3 times.

For co-immunoprecipitation, HEK cells were co-transfected with plasmids (6 μ g total) encoding myc-tagged or untagged LRRC8A and N-terminal fusion constructs of LRRC8A-E or CIC-1 (or soluble GFP) on 10-cm dishes using PEI as described above. 48 h post-transfection cells were lysed in 300 μ l lysis buffer (150 mM NaCl, 1% NP-40, 0.5% sodium deoxycholate, 50 mM Tris-HCl pH 7.5, 4 mM Pefabloc (Roth), complete proteinase inhibitor cocktail (Roche)) for 10 min on ice. The lysate was pre-cleared by centrifugation at 14,000 rpm for 10 min at 4°C and subsequently spun at 30,000 g for 30 min at 4°C. 150 μ l of the supernatant were mixed with 10 μ g of the respective antibody and IP buffer (150 mM NaCl, 0.1% NP-40; 0.05% sodium deoxycholate, 50 mM Tris-HCl, pH 7.5, complete proteinase inhibitor cocktail (Roche)) was added to final volume of 800 μ l. The sample was rotated for 1-2 h at 4°C before 10 μ l of Protein A Dynabeads® (Life Technologies) were added and rotation continued overnight at 4°C. After four washes with 500 μ l IP buffer, precipitates were eluted in 40 μ l Lämmli sample buffer, separated by SDS-PAGE and analyzed by Western blot as indicated. Lysate equivalent to 20% of input was loaded as reference. Experiments were repeated 3 times.

For the immunoprecipitation from native cells, lysates from two confluent 15-cm plates per cell-line (wild-type and *LRRC8A*^{-/-}) were prepared as described above. 1.9 ml lysate were mixed with equal volumes of IP buffer and 30 μ l of Protein A Dynabeads® (Life Technologies) previously coupled to 15 μ g of the LRRC8A antibody using dimethyl pimelimidate. After incubation and washing as described above, precipitates were eluted from the beads in 50 μ l of 0.2 M glycine (pH 2.5), mixed with Lämmli sample buffer, separated by SDS-PAGE and analyzed by Western blot as indicated.

To assess protein expression, cells were lysed as described above. Protein concentrations were determined by BCA and equal amounts were separated by SDS-PAGE and analyzed by Western blot as indicated.

Taurine Efflux Experiments

HEK or HCT116 cells were grown to ~80% confluency (48-72 h after plating) in 35-mm diameter plates coated with poly-L-lysine. For rescue experiments, cells were transfected one day before flux measurements with LRRC8A and LRRC8C-GFP expression plasmids using Fugene HD. For these experiments, WT cells were mock transfected with a GFP expression vector. Cells were loaded with $^3\text{[H]}$ -taurine (2 $\mu\text{Ci/ml}$; Perkin-Elmer) for 2 to 2.5 h in culture medium (without FCS) at 37°C. They were then washed 7 times at room temperature with isotonic solution (in mM: 150 NaCl, 6 KCl, 1 MgCl_2 , 1.5 CaCl_2 , 10 glucose, 10 HEPES pH 7.4, 320 mOsm). After washing, external media were removed in 5-min intervals and replaced with fresh isotonic or hypotonic solution (in mM: 105 NaCl, 6 KCl, 1 MgCl_2 , 1.5 CaCl_2 , 10 glucose, 10 HEPES pH 7.4, 240 mOsm) and saved for counting. At the end of the experiment, cells were lysed with 0.75 ml of 0.1 M NaOH. The radioactivity of cell supernatants and of the final cell lysate was determined in a liquid scintillation counter. Values presented were normalized to the total cellular radioactivity at that time point which was determined by adding the counts from the cell lysate and those of the supernatants collected at the corresponding and following time points. In each flux experiment, each data point represents the mean of 6 wells.

RVD Measurements

Cell volume was measured semiquantitatively using the calcein fluorescence method (38). HEK cells were plated 2 days before measurements at a density of 6,000 cells per well in a 384-well plate. For the RVD assay, 10 μM calcein-AM (Affymetrix eBioscience) in DMEM were loaded for 1 h at 37°C and then washed 3 times with 80 μl isotonic solution (in mM: 145 NaCl, 5 KCl, 1 MgCl_2 , 2 CaCl_2 , 10 glucose, 10 HEPES pH 7.4, 329 mOsm) using a Tecan Freedom EVO 200 workstation. Finally 10 μl of the isotonic solution were added to each well. After a 5-min incubation period the plate was transferred into the FLIPRTM (Molecular Devices) and fluorescence measurements at $\lambda = 515\text{-}575$ nm were initiated using the FLIPR Fluo4 LED/filter set. After baseline recording for 25 s, 25 μl aqua dest. were added to the wells resulting in a final osmolarity of 94 mOsm. Calcein fluorescence was monitored for ~65 min. Wells containing cells of the respective cell-line not loaded with calcein-AM (but otherwise treated equally) were used for background subtraction, and fluorescence values were normalized to $t = 30$ s (after the pipetting procedure). Less pronounced swelling and RVD of WT HEK cells was observed under the conditions of our primary screen (exposure to 189 mOsm) and RVD was likewise abolished in *LRRC8A*^{-/-} cells (*not shown*).

Author contributions:

F.K.V. and T.S. established and conducted the siRNA screen with K.L. and J.P.K., generated cell lines and antibodies, and designed, performed and analyzed molecular biological, biochemical and cell biological experiments. F.U. and J.M. designed, performed and analyzed patch-clamp experiments. D.L. performed taurine flux measurements. N.M. and M.A.A.-N. provided bioinformatics analysis. T.J.J. designed and analyzed experiments and wrote the paper with critical input of all authors.

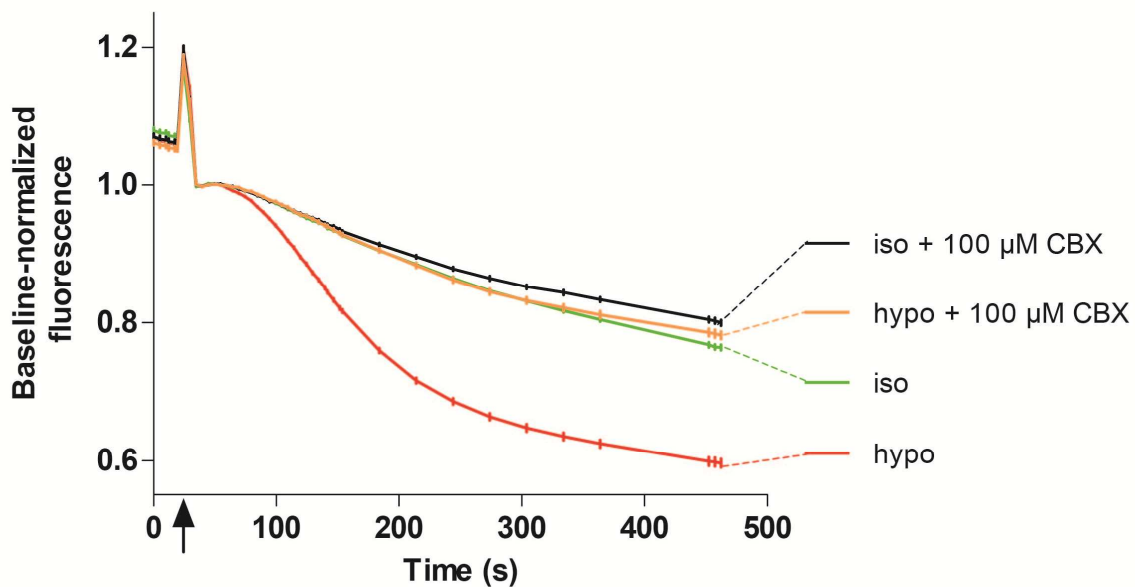
Supplementary Figures

Fig. S1. Effect of carbenoxolone on hypotonicity-induced YFP quenching by iodide. Fluorescence trace from a FLIPR™ experiment similar to those in Fig. 1C in which the effect of carbenoxolone (CBX), an inhibitor of VRAC and gap junctions (18), was investigated. Carbenoxolone was included in the I⁻-containing solution and added at the time point indicated by arrow.

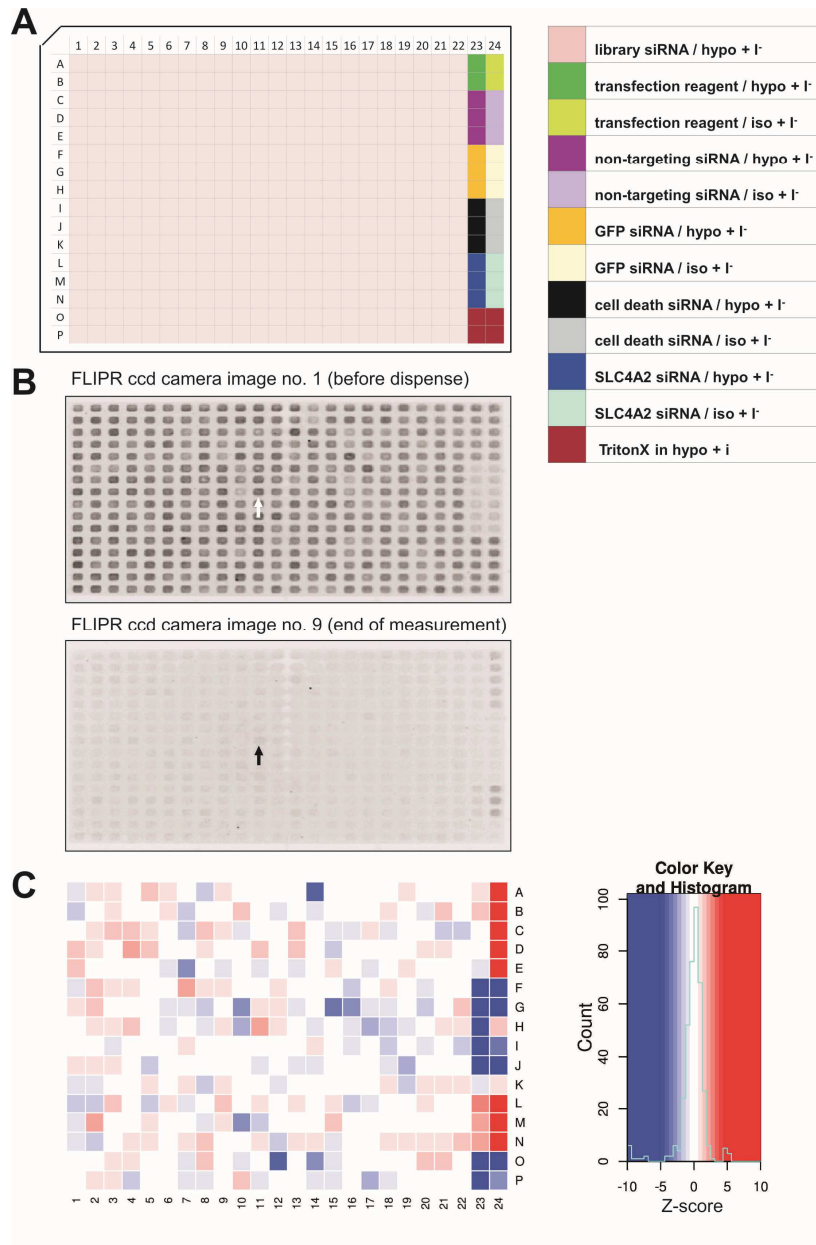


Fig. S2. Genome-wide RNA interference screen for VRAC. (A) Plate lay-out. Cells in wells of rows 1-22 were transfected with individual siRNAs of the Ambion Silencer[®] Human Genome siRNA Library V3 and tested for hypotonicity-induced YFP-quenching (experimental wells). Rows 23 and 24 contained control wells that were treated as indicated. (B) Photograph (inverted) of YFP fluorescence of an entire plate before the pipetting step (top) and at the end of the experiment (below). Note that fluorescence of cells treated with siRNA against YFP and cell-death inducing siRNA is strongly reduced at the beginning of the experiment (top) (transfection control). At the end of the experiment (bottom), fluorescence has remained strong in wells remaining in isotonic solution throughout. Arrows indicate well H11 containing cells transfected with the most efficient siRNA against *LRRC8A*. (C) Heat map of the same plate. Z-scores for S_{\max} (maximal slope of quenching) are displayed using the color scale shown at right.

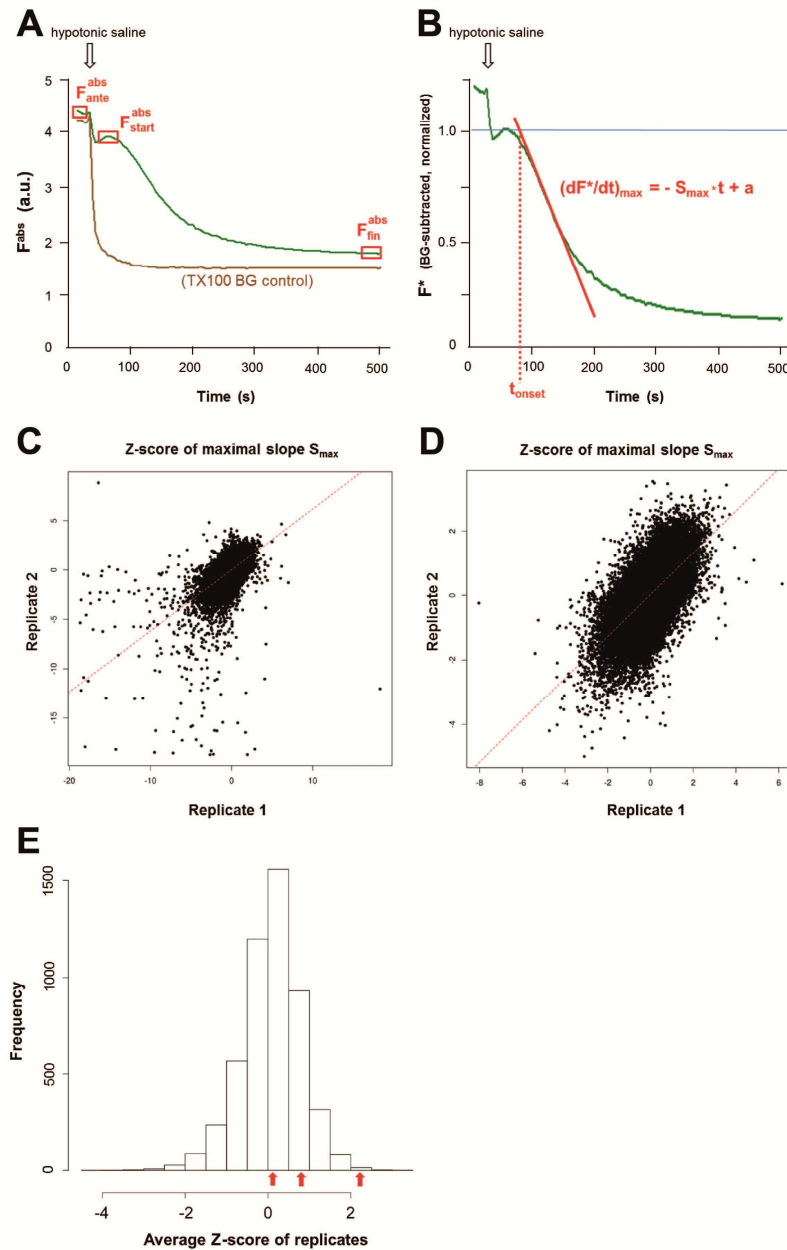


Fig. S3. Analysis of the primary, genome-wide siRNA screen for VRAC. (A and B) Parameters derived from the primary siRNA screen for VRAC. (A) Example of original data obtained from the FLIPRTM primary genome-wide screen, showing the absolute, non-corrected values of fluorescence (F^{abs}) measured at $\lambda = 526-585$ nm as a function of time. The **green** curve shows a representative trace from an experimental well with YFP-expressing HEK cells that have been treated with siRNA and were exposed to hypotonic, iodide-containing solution at the time indicated by the arrow. The **brown** curve shows a control well from the same plate to which hypotonic, iodide-containing solution containing 1% Triton X100. (B) Background-subtracted and normalized fluorescence F^* . After subtracting the background determined in control wells treated with Triton X100, the fluorescence of

every experimental well was normalized to its individual $F_{\text{start}}^{\text{abs}}$ value. The maximal slope of fluorescence decrease S_{max} was determined by linear regression to the curve between 35 and 300 seconds and was used as main parameter to identify hits. t_{onset} was defined as indicated and can be used as measure of the speed of signal transduction between volume increase and VRAC opening. **(C and D)** Fidelity of replicate screens. Correlation of Z-scores of maximal slope S_{max} between the original and the replicate screen observed with all 65,061 siRNAs (C) and after filtering out those measurements that were flagged for low cell number or did not reach near-steady-state fluorescence by the end of the measurement (D). Z-scores from screen 1 and screen 2 are plotted on the x- and y-axis, respectively. The Pearson correlation coefficient ($r=0.62$ and $r=0.65$, respectively) indicates positive correlation between replicate screens. The regression line from simple linear regression is shown as a dashed red line. The elimination of outliers demonstrated the usefulness of these warning flags. **(E)** Histogram of Z-scores for maximal slope (S_{max}) from the genome-wide siRNA screen. Measurements which were flagged for low cell number or did not reach steady state fluorescence by the end of measurement were filtered out, resulting in values for 50,258 siRNAs. The averaged Z-scores from screen 1 and screen 2 are plotted. Arrows indicate the Z-scores of three individual siRNAs against *LRRC8A* (0.125, 0.809 and 2.217).

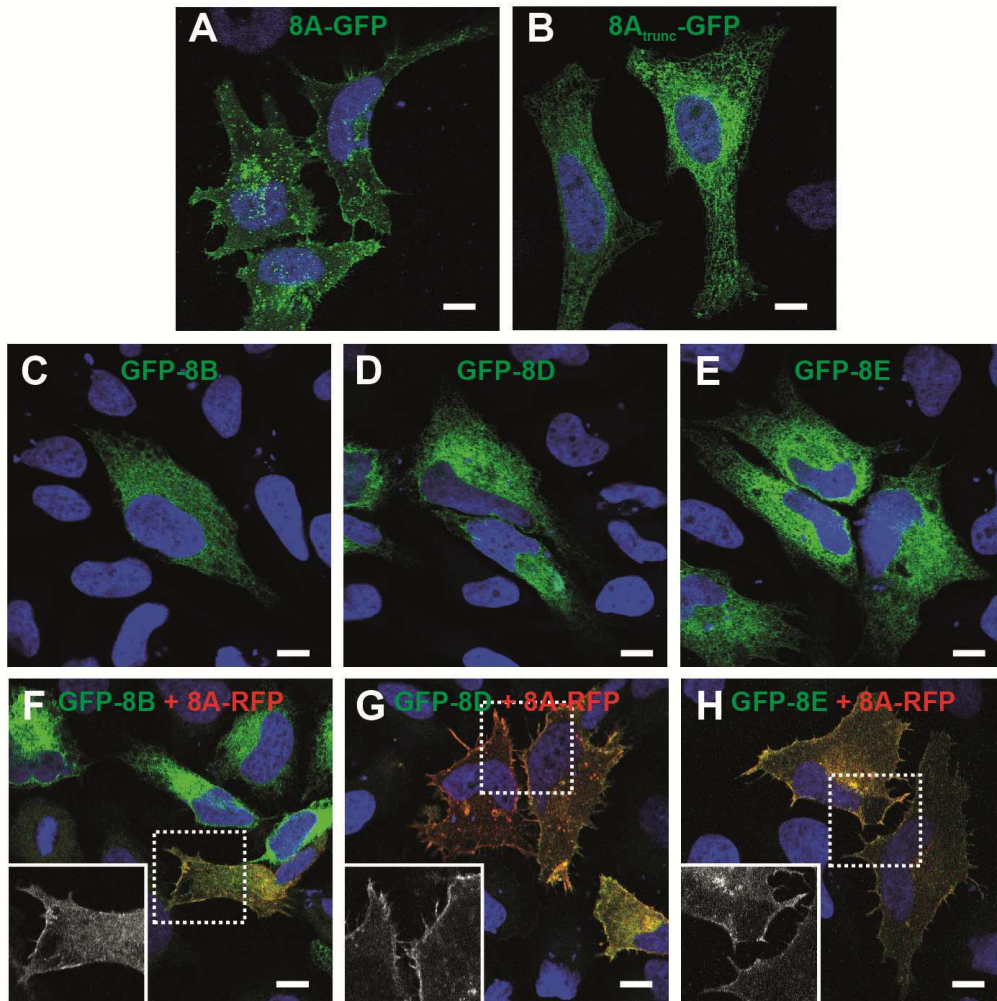


Fig. S4. Subcellular localization of LRRC8 proteins. (A) Plasma membrane localization of LRRC8A-GFP transfected into HeLa cells detected by GFP labeling. (B) Truncated LRRC8A fused at R719 to GFP failed to reach the plasma membrane. This truncation mimics the effect of a chromosomal translocation at the *LRRC8A* that was found in a patient with agammaglobulinemia (21). (C-E) Intracellular localization of LRRC8B, D and E when transfected alone (for LRRC8C, see Fig 1I). (F-H) LRRC8B, D and E reach the plasma membrane when co-transfected with LRRC8A (for LRRC8C, see Fig 1J). Insets, magnification of boxed areas showing exclusively GFP fluorescence. Scale bar, 10 μ m for all panels.

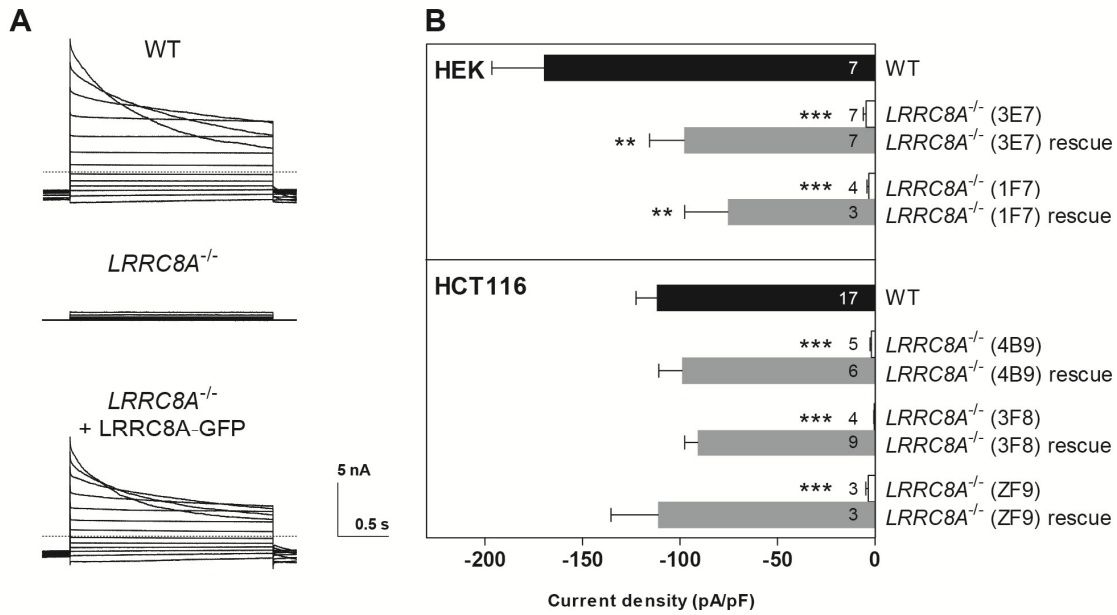


Fig. S5. Absence of $I_{Cl(swell)}$ in independent *LRRRC8A*^{-/-} cell lines. (A) Example $I_{Cl(swell)}$ traces (as in Fig. 1E, but 2-s pulses) of WT and mutant HEK cells (clone 3E7). When transfected into HEK *LRRRC8A*^{-/-} cells, LRRRC8A rescues $I_{Cl(swell)}$. (B) Amplitudes of maximally activated $I_{Cl(swell)}$ (at -80 mV) of WT HEK, WT HCT116 and different *LRRRC8A*^{-/-} cell lines, rescued by transfection of LRRRC8A-GFP cDNA. Note that the amplitude of $I_{Cl(swell)}$ current was not fully rescued in HEK cells by LRRRC8-GFP transfection, an observation that fits to the suppression of $I_{Cl(swell)}$ from native HEK cells by LRRRC8A transfection (Fig. 1F). Mean currents \pm SEM, number of measurements is indicated. **, $p < 0.01$ and ***, $p < 0.001$ compared to WT HEK or WT HCT116, respectively. For description of different cell lines see table S4.

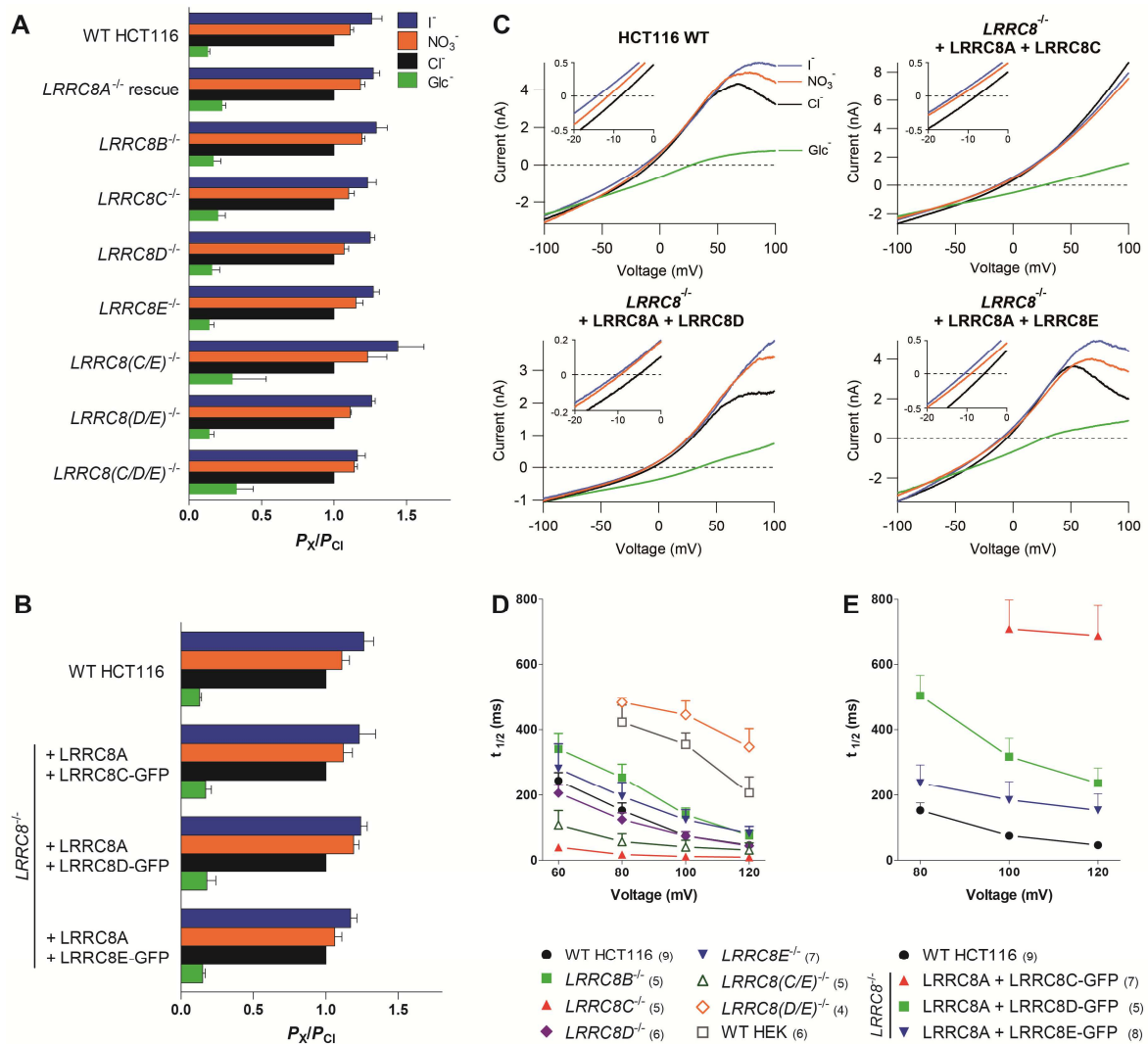


Fig. S6. Characterization of $I_{Cl(swell)}$ in HCT116 cells. (A) Relative anion permeabilities (P_x/P_{Cl}) as determined from shifts in reversal potential of $I_{Cl(swell)}$ upon anion substitution in WT, *LRRC8* knock-out HCT116 cell lines, and (B) *LRRC8*^{-/-} cells transfected with the combinations indicated. Mean \pm SEM, number of cells \geq 4. (C) Example current-voltage relationships obtained at the time of maximal current activation of endogenous and reconstituted $I_{Cl(swell)}$ with normal and anion substituted hypotonic extracellular solutions. Insets show a magnification of reversal potentials for Cl⁻, I⁻ and NO₃⁻. The reversal potential is shifted to slightly more negative voltages when extracellular Cl⁻ is replaced by I⁻ and NO₃⁻ and to drastically more positive voltages upon replacement by D-gluconate. (D-E) Voltage-dependent $I_{Cl(swell)}$ inactivation assessed by time needed to inactivate to 50% of the difference between currents at end / beginning of pulse (I_{2sec}/I_{max}). In panel E, constructs were transfected into the quintuple KO HCT116 cell line (*LRRC8*^{-/-}). Numbers in brackets indicate the number of cells measured.

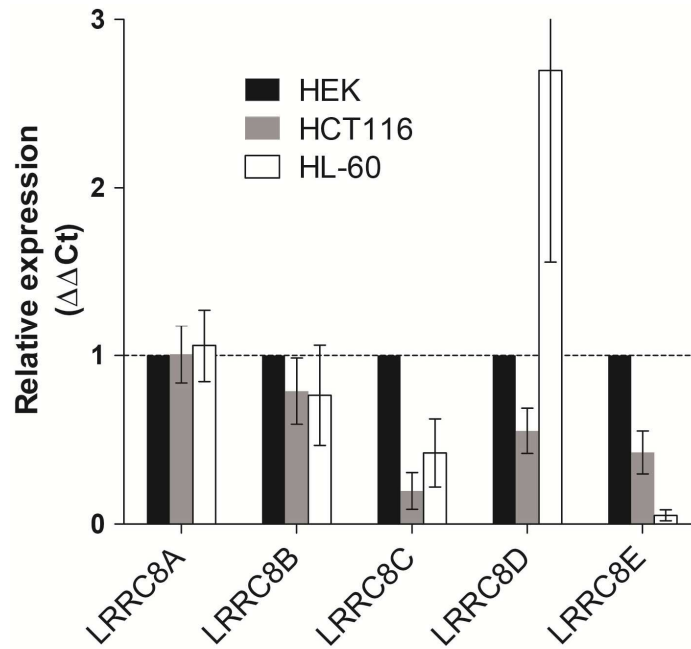


Fig S7. Relative LRRRC8 mRNA expression. LRRRC8A – E mRNA expression in HEK, HCT116, and HL-60 cells determined by quantitative RT-PCR. Values were normalized to the respective value of HEK cells. Values represent the means from 4 experiments. Error bars indicate SEM.

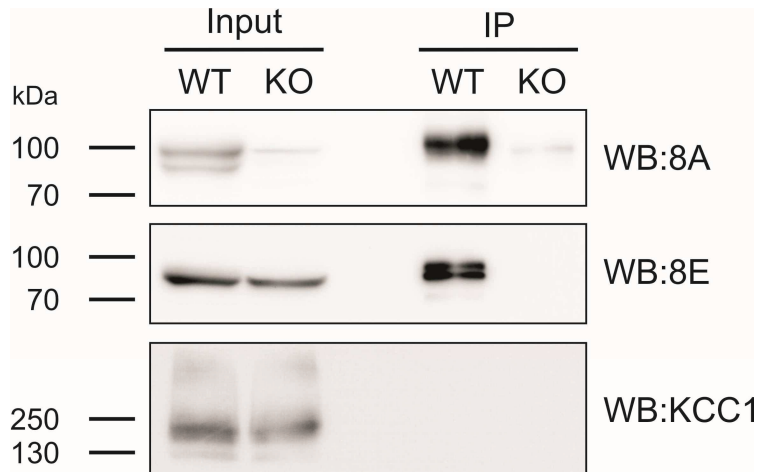


Fig. S8. Heteromerization of endogenous LRRRC8 proteins. LRRRC8A co-precipitated LRRRC8E (for which a suitable antibody was available) in immunoprecipitation with an LRRRC8A antibody from wild-type (WT) HEK cell lysate, but not from the *LRRRC8A*^{-/-} knockout (KO, clone 3E7). The plasma membrane ion transporter KCC1 (negative control) did not co-precipitate with LRRRC8A. Lysate equivalent to 25% of input was loaded as reference (input).

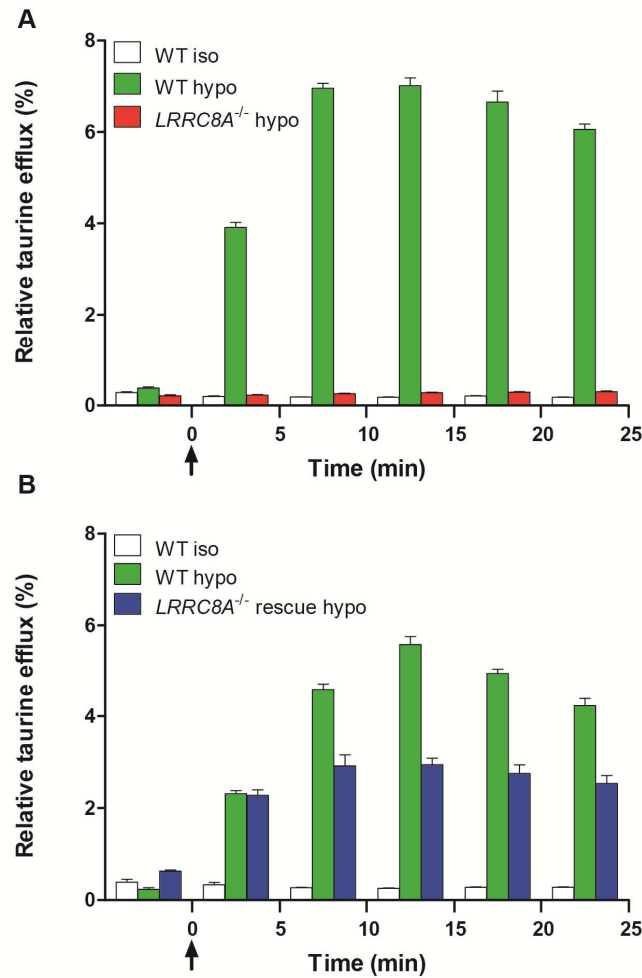


Fig. S9. LRRC8A is crucial for swelling-induced ³[H]-taurine efflux in HEK cells. (A) One set of wild-type (WT) HEK cells were in isotonic solution throughout, whereas another set of WT or *LRRC8A*^{-/-} HEK cells were exposed to hypotonic solution starting at t=0 (arrow). Bars represent means of 6 measurements of taurine efflux between the indicated time points. Error bars indicate SEM. (B) Taurine efflux measurement as in (A), but the *LRRC8A*^{-/-} HEK cells had been co-transfected with LRRC8A and LRRC8C-GFP. This co-transfection partially restores the taurine flux capability of *LRRC8A*^{-/-} HEK cells. Co-transfection was necessary as overexpression of LRRC8A alone leads to a suppression of $I_{Cl(swell)}$. Only partial rescue of fluxes with transfected cells agrees with the transfection efficiency of roughly 50%.

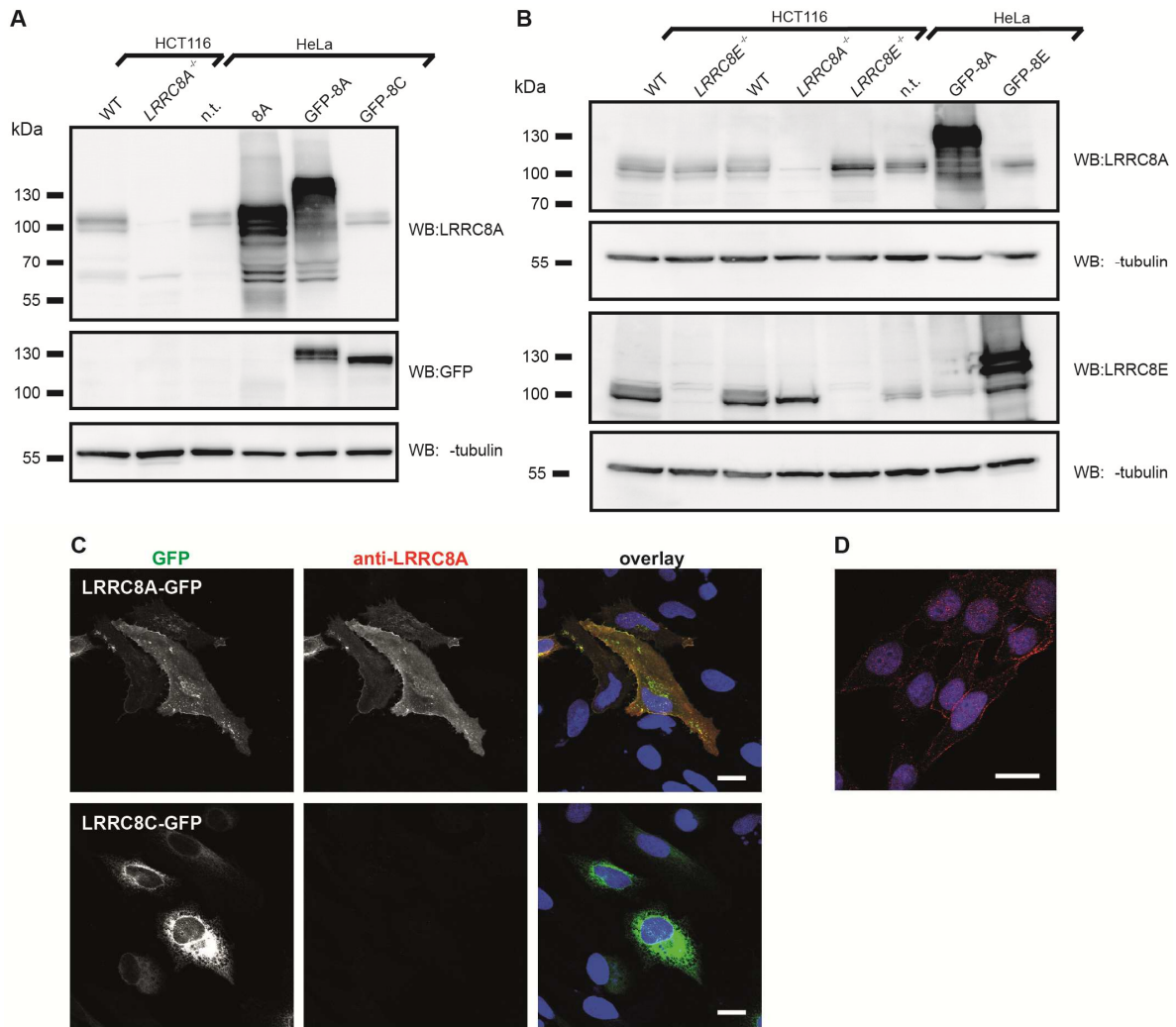


Fig. S10. Characterization of LRRC8A and LRRC8E antibodies. (A) Western blots of lysates from wild-type (WT) and *LRRC8A*^{-/-} (clone 3F8) HCT116 cells, and from HeLa cells that were not transfected (n.t.), or transfected with LRRC8A or with LRRC8A and LRRC8C GFP fusion proteins were probed with the LRRC8A antibody, or antibodies against GFP and α -tubulin (loading control) as indicated. The LRRC8A antibody recognizes native and overexpressed LRRC8A specifically. (B) Western blots of lysates from WT, *LRRC8A*^{-/-} (clone 4B9) and *LRRC8E*^{-/-} (clones BCDE(WT)-F5 and CE(WT)-B6) HCT116 cells, and from HeLa cells that were not transfected (n.t.) or transfected with LRRC8A or LRRC8E GFP fusion proteins were probed with antibodies against LRRC8A, LRRC8E and α -tubulin. The LRRC8E antibody recognizes specifically native and overexpressed LRRC8E, whereas LRRC8E is not recognized by the LRRC8A antibody. (C) HeLa cells methanol-fixed and immunostained with the LRRC8A antibody (red in overlay) 24 h after transfection with LRRC8A (upper panel) and LRRC8C (bottom panel) GFP fusion proteins (GFP signal, green in overlay), nuclei in blue. The LRRC8A antibody recognizes specifically overexpressed LRRC8A. Scale bars, 20 μ m. (D) Higher exposure of non-transfected HeLa cells reveals plasma membrane staining with the LRRC8A antibody (red; nuclei in blue). Scale bar, 20 μ m.

Supplementary Tables

Table S1. List of anion transporters tested by siRNA interference in HEK cells in a FLIPR™ prescreen.

Gene name	Alternative name(s)	Proposed function
<i>ANO1</i>	Anoctamin1, TMEM16A	Ca ²⁺ -activated Cl ⁻ channel
<i>ANO3</i>	Anoctamin3, TMEM16C	Ca ²⁺ -activated Cl ⁻ channel (?)
<i>ANO4</i>	Anoctamin4, TMEM16D	Ca ²⁺ -activated Cl ⁻ channel (?)
<i>ANO5</i>	Anoctamin5, TMEM16E	Ca ²⁺ -activated Cl ⁻ channel (?)
<i>ANO6</i>	Anoctamin6, TMEM16F	Ca ²⁺ -activated Cl ⁻ or cation channel, scramblase
<i>ANO7</i>	Anoctamin7, TMEM16G	Ca ²⁺ -activated Cl ⁻ channel (?)
<i>ANO8</i>	Anoctamin8, TMEM16H	Ca ²⁺ -activated Cl ⁻ channel (?)
<i>ANO9</i>	Anoctamin9, TMEM16J	Ca ²⁺ -activated Cl ⁻ channel (?)
<i>ANO10</i>	Anoctamin10, TMEM16K	Ca ²⁺ -activated Cl ⁻ channel (?)
<i>CLCN3</i>	CIC-3	Cl ⁻ /H ⁺ -exchanger, wrongly claimed to be VRAC
<i>BEST1</i>	Bestrophin 1	Ca ²⁺ -activated Cl ⁻ channel
<i>BEST2</i>	Bestrophin 2	Ca ²⁺ -activated Cl ⁻ channel
<i>SLC4A2</i>	AE2, anion exchanger 2	Cl ⁻ /HCO ₃ ⁻ exchanger
<i>SLC4A3</i>	AE3, anion exchanger 3	Cl ⁻ /HCO ₃ ⁻ exchanger
<i>SLC12A2</i>	NKCC1	NaK2Cl cotransporter
<i>SLC12A4</i>	KCC1	KCl cotransporter
<i>SLC12A6</i>	KCC3	KCl cotransporter
<i>SLC12A7</i>	KCC4	KCl cotransporter
<i>SLC26A1</i>	SAT1	anion exchanger, sulfate transporter
<i>SLC26A9</i>		anion transporter
<i>SLC26A11</i>	KBAT	Na ⁺ -dependent sulfate transporter, Cl ⁻ channel (?)

Table S2. List of candidate genes from genome-wide siRNA screen that were taken into a secondary FLIPR™ RNA interference screen using SMARTpools of independent siRNAs.

Gene ID	Gene symbol	TMDs*	Z-score†	Gene ID	Gene symbol	TMDs*	Z-score†		
1	3371	<i>TNC</i>	1	2.6931	45	51338	<i>MS4A4A</i>	4	1.3255
2	79652	<i>TMEM204</i>	4	2.3119	46	92255	<i>DKFZp434H2226</i>	9	1.3153
3	253558	<i>ALCAT1</i>	3	2.1069	47	79762	<i>FLJ14146</i>	1	1.3139
4	54879	<i>ST7L</i>	2	1.9163	48	159371	<i>TMEM20</i>	10	1.3091
5	5793	<i>PTPRG</i>	1	1.8685	49	79683	<i>ZDHHC14</i>	4	1.3016
6	28959	<i>LR8 / TMEM176B</i>	4	1.8351	50	65062	<i>ALS2CR4</i>	4	1.2954
7	51234	<i>EMC4</i>	2	1.7410	51	79844	<i>ZDHHC11</i>	5	1.2780
8	10098	<i>TM4SF9/TSPAN5</i>	4	1.7358	52	10100	<i>TSPAN-2</i>	4	1.2743
9	125111	<i>GJC1/GJD3</i>	4	1.7326	53	123606	<i>NIPA1</i>	8	1.2581
10	29940	<i>SART2</i>	3	1.6643	54	55362	<i>TMEM63B</i>	11	1.2448
11	284723	<i>SLC25A34</i>	2	1.6399	55	124491	<i>TMEM170A</i>	3	1.2369
12	130814	<i>PQLC3</i>	4	1.6306	56	56674	<i>TMEM9B</i>	2	1.2335
13	23505	<i>RW1/TMEM131</i>	2	1.6096	57	94015	<i>TTYH2</i>	6	1.2300
14	199953	<i>TMEM201</i>	6	1.5948	58	203562	<i>TMEM31</i>	2	1.2116
15	80759	<i>KHDC1</i>	2	1.5846	59	27069	<i>GHITM</i>	6	1.2099
16	9415	<i>FADS2</i>	4	1.5817	60	26526	<i>TM4-B</i>	3	1.1928
17	57484	<i>RNF150</i>	2	1.5569	61	81671	<i>VMP1</i>	6	1.1703
18	54741	<i>OBRGRP</i>	4	1.5488	62	374882	<i>TMEM205</i>	4	1.1329
19	5348	<i>FXYD1</i>	1	1.5477	63	10712	<i>Fam189B</i>	4	1.1222
20	56172	<i>ANKH</i>	8	1.5316	64	85414	<i>Prostein/SLC45A3</i>	11	1.1208
21	4034	<i>LRCH4</i>	1	1.5303	65	91147	<i>TMEM67</i>	4	1.1122
22	57198	<i>ATP8B2</i>	9	1.5268	66	57348	<i>TTYH1</i>	5	1.0725
23	53346	<i>TM6SF1</i>	9	1.5216	67	128506	<i>OCSTAMP</i>	6	1.0707
24	120224	<i>TMEM45B</i>	5	1.5205	68	55852	<i>TEX2</i>	2	1.0702
25	56262	<i>LRRRC8A</i>	4	1.5129	69	93109	<i>TMEM44</i>	4	1.0630
26	10959	<i>RNP24</i>	2	1.4911	70	11161	<i>C14orf1</i>	4	1.0598
27	79022	<i>TMEM106C</i>	2	1.4885	71	64137	<i>ABCG4</i>	7	1.0392
28	349149	<i>GJE1/GJC3</i>	3	1.4769	72	29097	<i>HSPC163</i>	3	1.0315
29	746	<i>TMEM258</i>	2	1.4751	73	55625	<i>ZDHHC7</i>	4	1.0268
30	53827	<i>FXYD5</i>	1	1.4684	74	64429	<i>ZDHHC6</i>	4	1.0165
31	55009	<i>C19orf24</i>	2	1.4654	75	54860	<i>MS4A12</i>	4	1.0130
32	29058	<i>C20orf30</i>	2	1.4566	76	162427	<i>FAM134C</i>	3	1.0120
33	10099	<i>TM4SF8/ TSPAN3</i>	4	1.4361	77	23460	<i>ABCA6</i>	13	1.0099
34	54929	<i>TMEM161A</i>	8	1.4268	78	9906	<i>SLC35E2</i>	3	0.9891
35	84561	<i>SLC12A8</i>	10	1.4140	79	64645	<i>HIAT1</i>	12	0.9848
36	113829	<i>SLC35A4</i>	9	1.4016	80	345274	<i>SOAT/SLC10A6</i>	8	0.9758
37	29956	<i>LASS2</i>	5	1.3728	81	347735	<i>TDE2L/SERINC2</i>	11	0.9695
38	145407	<i>C14orf37</i>	2	1.3710	82	55002	<i>TMCO3</i>	10	0.9674
39	51522	<i>TMEM14C</i>	4	1.3670	83	202915	<i>TMEM184A</i>	7	0.9488
40	55739	<i>FLJ10769</i>	1	1.3656	84	8082	<i>SSPN</i>	4	0.9236
41	284099	<i>C17orf78</i>	1	1.3551	85	84548	<i>FAM11A/TMEM185A</i>	8	0.9025
42	81555	<i>SMAP-5</i>	4	1.3487	86	135656	<i>DPCR1</i>	2	0.8911
43	57181	<i>SLC39A10</i>	7	1.3480	87	85013	<i>TMEM128</i>	4	0.7763
44	7355	<i>SLC35A2</i>	8	1.3401					

*predicted number of transmembrane domains

†mean Z-score for S_{\max} of the two 'best' siRNAs from 2 replicate primary screens

Table S3. Clonal cell lines with disrupted *LRRC8* genes.

Cell line	Clone name	Construct used*	Genetic modification	Protein modification	Used for figure
<i>LRRC8A</i> ^{-/-} (HEK)	3E7	3A	a1: Δ21nt (t110-a130) a2: insertion of 1 nt (t after c123)	A1: ΔM37-G43 in TMD1 (non-functional) A2: G42W-fs in TMD1	Fig. 1H; Fig. 2A; Fig. 4B; fig. S5; fig. S8; fig. S9
	1F7	1A	a1: Δ9nt (a958-g966) a2: Δ2nt (c965-g966) a3: Δ23nt (a958-g980)	A1: ΔI320-A322 at start of TMD4(non-functional) A2: A322V-fs at start of TMD4 A3: I320P-fs at start of TMD4	Fig. 2A; fig. S5B
<i>LRRC8A</i> ^{-/-} (HCT116)	3F8	3A	Δ2g out of 6g (g124-g129)	G43D-fs in TMD1	Fig. 2A, 2B, 2C; fig. S5B; fig. S6A; fig. S10A
	4B9	4A	a1: Δ32nt (c195-g226) a2: duplication of t206	A1: C65W-fs between TMD1 and TMD2 A2: R70P-fs between TMD1 and TMD2	Fig. 2A; Fig. 4A; fig. S5B; fig. S10B
	ZF9	ZFN	a1: Δ2nt (a508-c509) a2: insertion of 5nt (cacga after a511)	A1: T170E-fs between TMD2 and TMD3 A2: R171T-fs between TMD2 and TMD3	Fig. 2A; fig. S5B
<i>LRRC8B</i> ^{-/-} (HCT116)	n2B-D3	2B	duplication of t446	E150R-fs after TMD2	Fig. 2B, 2C, 2D; fig. S6A, S6D
<i>LRRC8C</i> ^{-/-} (HCT116)	n1C-C2	1C	duplication of t119	F41V-fs in TMD1	Fig. 2B, 2C, 2D; fig. S6A, S6D
<i>LRRC8D</i> ^{-/-} (HCT116)	n1D-F11	1D	a1: Δ19nt (a325-t343) a2: duplication of a325	D1: P110L-fs between TMD1 and TMD2 D2: I109N-fs between TMD1 and TMD2	Fig. 2B, 2D; fig. S6D data from both clones pooled for: Fig. 2C fig. S6A
	n1D-B2	1D	duplication of a325	I109N-fs between TMD1 and TMD2	
<i>LRRC8E</i> ^{-/-} (HCT116)	BCDE(WT)-F5	1E	duplication of a94	T32N-fs in TMD1	Fig. 2B; fig. S6A both clones: fig. S10B data from both clones pooled for: Fig. 2C, 2D; fig. S6D
	CE(WT)-B6	1E	duplication of a94	T32N-fs in TMD1	
<i>LRRC8(D/E)</i> ^{-/-} (HCT116)	nBCDE (WT)-G9	1D, 1E	D: duplication of a325 E: duplication of a94	D: I109N-fs between TMD1 and TMD2 E: T32N-fs in TMD1	Fig. 2B; fig. S6A
	nBCDE (WT)-B3	1D, 1E	D: duplication of a325 E: duplication of a94	D: I109N-fs between TMD1 and TMD2 E: T32N-fs in TMD1	data from both clones pooled for: Fig. 2C, 2D; fig. S6D
<i>LRRC8(C/E)</i> ^{-/-} (HCT116)	BCDE(WT)- F5+1C-D5	1C, 1E	C: a1: duplication of t119 a2: Δ5nt (c114-g118) and duplication of t119 E: duplication of a94	C1: F41V-fs in TMD1 C2: G39C-fs in TMD1 E: T32N-fs in TMD1	Fig. 2B, 2C, 2D; fig. S6A, S6D
<i>LRRC8(C/D/E)</i> ^{-/-} (HCT116)	nBCDE(WT)-H8	1B, 1C, 1D, 1E	B: heterozygous duplication of a1043 C: 78nt (from a66 onwards) incl. splice acceptor site replaced by 13 nt (net Δ65nt) D: a1: duplication of a325 a2: Δ11nt (g322-t332) E: a1: duplication of a94 a2: Δ10nt (g87-c96)	C: W23R-fs at start of TMD1, before missing splice site D1: I109N-fs between TMD1 and TMD2 D2: D108Q-fs between TMD1 and TMD2 E1: T32N-fs in TMD1 E2: Y30W-fs in TMD1	Fig. 2B, 2C
<i>LRRC8(B/C/D/E)</i> ^{-/-} (HCT116)	BCDE (WT2)-D2+2B-E8	2B, 1C, 1D, 1E	B: a1: duplication of t446 a2: Δ2nt (c447-g448) C: duplication of t119 D: duplication of a325 E: Δ2nt (t92-c93)	B1: E150R-fs after TMD2 B2: E150A-fs after TMD2 C: F41V-fs in TMD1 D: I109N-fs between TMD1 and TMD2 E: L31H-fs in TMD1	Fig. 2B, 2C; Fig. 4A
<i>LRRC8</i> ^{-/-} (HCT116)	BC+DE (KO)D5+ 2B-G4	3A, 2B, 1B [§] , 1C, 1D, 1E	A: Δ2g out of 6g (g124-g129)	A: G43D-fs in TMD1	Fig. 2E, 2F, 2G; fig. S6B, S6C, S6E
			B: a1: duplication of t446 a2: Δ4nt (c447-g450)	B1: E150R-fs after TMD2 B2: E150I-fs after TMD2	
			C: duplication of t119	C: F41V-fs in TMD1	
			D: duplication of a325	D: I109N-fs between TMD1 and TMD2	
			E: duplication of a94	E: T32N-fs in TMD1	

a = allele (only given if alleles differed in modifications); fs = frameshift; nt = nucleotide; TMD = transmembrane domain; ZFN = zinc-finger nuclease; Δ = deletion
Indicated nucleotide numbers give nucleotide position within the ORF.

* For targeted guide sequences, see table S4.

[§] Targeting with construct 1B in *LRRC8*^{-/-} cell line resulted in a duplication of a1043 which would lead to A349G-fs after TMD4. However, the mutations by the 2B targeting (given in table) truncate *LRRC8B* already after TMD2.

Table S4. Guide sequences used for the generation of knock-out cell lines with the CRISPR/Cas system.

Target gene	Construct	Guide sequence (5'→3')	Targeting strand	Target location in protein
<i>LRRC8A</i>	1A	ggctgatgtagaaggacgcc <u>agg</u>	-	aa 320-328 (beginning of TMD4)
	3A	tgatgattgccgtcttcg <u>ggggg</u>	+	aa 36-43 (in TMD2)
	4A	tcctgcaatgattcgttcc <u>ggg</u>	+	aa 64-71 (between TMD1 and TMD2)
<i>LRRC8B</i>	1B	ttttctttaacgcctca <u>agg</u>	-	aa 346-353 (after TMD4)
	2B	ggccacaaaatgctcgagcct <u>gg</u>	-	aa 147-354 (between TMD2 and TMD3)
<i>LRRC8C</i>	1C	atgctcatgatcggcgtt <u>gg</u>	+	aa 35-42 (in TMD1)
<i>LRRC8D</i>	1D	gtggctctgagaggtatgc <u>agg</u>	-	aa 107-114 (between TMD1 and TMD2)
<i>LRRC8E</i>	1E	gctggccgagtacctcaccg <u>gg</u>	+	aa 27-34 (in TMD1)

aa= amino acid; TMD = transmembrane domain; PAM sequences are underlined

References and Notes

1. E. K. Hoffmann, I. H. Lambert, S. F. Pedersen, Physiology of cell volume regulation in vertebrates. *Physiol. Rev.* **89**, 193–277 (2009). [Medline](#) [doi:10.1152/physrev.00037.2007](https://doi.org/10.1152/physrev.00037.2007)
2. H. Pasantes-Morales, R. A. Lezama, G. Ramos-Mandujano, K. L. Tuz, Mechanisms of cell volume regulation in hypo-osmolality. *Am. J. Med.* **119** (suppl. 1), S4–S11 (2006). [Medline](#) [doi:10.1016/j.amjmed.2006.05.002](https://doi.org/10.1016/j.amjmed.2006.05.002)
3. B. Nilius, J. Eggermont, T. Voets, G. Buyse, V. Manolopoulos, G. Droogmans, Properties of volume-regulated anion channels in mammalian cells. *Prog. Biophys. Mol. Biol.* **68**, 69–119 (1997). [Medline](#) [doi:10.1016/S0079-6107\(97\)00021-7](https://doi.org/10.1016/S0079-6107(97)00021-7)
4. Y. Okada, K. Sato, T. Numata, Pathophysiology and puzzles of the volume-sensitive outwardly rectifying anion channel. *J. Physiol.* **587**, 2141–2149 (2009). [Medline](#) [doi:10.1113/jphysiol.2008.165076](https://doi.org/10.1113/jphysiol.2008.165076)
5. Y. Okada, Volume expansion-sensing outward-rectifier Cl⁻ channel: Fresh start to the molecular identity and volume sensor. *Am. J. Physiol.* **273**, C755–C789 (1997). [Medline](#)
6. P. S. Jackson, K. Strange, Volume-sensitive anion channels mediate swelling-activated inositol and taurine efflux. *Am. J. Physiol.* **265**, C1489–C1500 (1993). [Medline](#)
7. K. Strange, P. S. Jackson, Swelling-activated organic osmolyte efflux: A new role for anion channels. *Kidney Int.* **48**, 994–1003 (1995). [Medline](#) [doi:10.1038/ki.1995.381](https://doi.org/10.1038/ki.1995.381)
8. I. H. Lambert, E. K. Hoffmann, Cell swelling activates separate taurine and chloride channels in Ehrlich mouse ascites tumor cells. *J. Membr. Biol.* **142**, 289–298 (1994). [Medline](#) [doi:10.1007/BF00233436](https://doi.org/10.1007/BF00233436)
9. D. B. Shennan, Swelling-induced taurine transport: Relationship with chloride channels, anion-exchangers and other swelling-activated transport pathways. *Cell. Physiol. Biochem.* **21**, 15–28 (2008). [Medline](#) [doi:10.1159/000113743](https://doi.org/10.1159/000113743)
10. A. Stutzin, R. Torres, M. Oporto, P. Pacheco, A. L. Eguiguren, L. P. Cid, F. V. Sepúlveda, Separate taurine and chloride efflux pathways activated during regulatory volume decrease. *Am. J. Physiol.* **277**, C392–C402 (1999). [Medline](#)
11. T. Moser, R. H. Chow, E. Neher, Swelling-induced catecholamine secretion recorded from single chromaffin cells. *Pflugers Arch.* **431**, 196–203 (1995). [Medline](#) [doi:10.1007/BF00410191](https://doi.org/10.1007/BF00410191)
12. Y. Okada, T. Shimizu, E. Maeno, S. Tanabe, X. Wang, N. Takahashi, Volume-sensitive chloride channels involved in apoptotic volume decrease and cell death. *J. Membr. Biol.* **209**, 21–29 (2006). [Medline](#) [doi:10.1007/s00232-005-0836-6](https://doi.org/10.1007/s00232-005-0836-6)
13. S. Gründer, A. Thiemann, M. Pusch, T. J. Jentsch, Regions involved in the opening of CIC-2 chloride channel by voltage and cell volume. *Nature* **360**, 759–762 (1992). [Medline](#) [doi:10.1038/360759a0](https://doi.org/10.1038/360759a0)
14. S. C. Stotz, D. E. Clapham, Anion-sensitive fluorophore identifies the Drosophila swell-activated chloride channel in a genome-wide RNA interference screen. *PLOS ONE* **7**, e46865 (2012). [Medline](#) [doi:10.1371/journal.pone.0046865](https://doi.org/10.1371/journal.pone.0046865)
15. L. T. Chien, H. C. Hartzell, Rescue of volume-regulated anion current by bestrophin mutants with altered charge selectivity. *J. Gen. Physiol.* **132**, 537–546 (2008). [Medline](#) [doi:10.1085/jgp.200810065](https://doi.org/10.1085/jgp.200810065)

16. R. Fischmeister, H. C. Hartzell, Volume sensitivity of the bestrophin family of chloride channels. *J. Physiol.* **562**, 477–491 (2005). [Medline doi:10.1113/jphysiol.2004.075622](#)
17. L. J. Galletta, P. M. Haggie, A. S. Verkman, Green fluorescent protein-based halide indicators with improved chloride and iodide affinities. *FEBS Lett.* **499**, 220–224 (2001). [Medline doi:10.1016/S0014-5793\(01\)02561-3](#)
18. V. Benfenati, M. Caprini, G. P. Nicchia, A. Rossi, M. Dovizio, C. Cervetto, M. Nobile, S. Ferroni, Carbenoxolone inhibits volume-regulated anion conductance in cultured rat cortical astroglia. *Channels* **3**, 323–336 (2009). [Medline doi:10.4161/chan.3.5.9568](#)
19. K. Kubota, J. Y. Kim, A. Sawada, S. Tokimasa, H. Fujisaki, Y. Matsuda-Hashii, K. Ozono, J. Hara, LRRC8 involved in B cell development belongs to a novel family of leucine-rich repeat proteins. *FEBS Lett.* **564**, 147–152 (2004). [Medline doi:10.1016/S0014-5793\(04\)00332-1](#)
20. F. Abascal, R. Zardoya, LRRC8 proteins share a common ancestor with pannexins, and may form hexameric channels involved in cell-cell communication. *Bioessays* **34**, 551–560 (2012). [Medline doi:10.1002/bies.201100173](#)
21. A. Sawada, Y. Takihara, J. Y. Kim, Y. Matsuda-Hashii, S. Tokimasa, H. Fujisaki, K. Kubota, H. Endo, T. Onodera, H. Ohta, K. Ozono, J. Hara, A congenital mutation of the novel gene LRRC8 causes agammaglobulinemia in humans. *J. Clin. Invest.* **112**, 1707–1713 (2003). [Medline doi:10.1172/JCI18937](#)
22. L. Cong, F. A. Ran, D. Cox, S. Lin, R. Barretto, N. Habib, P. D. Hsu, X. Wu, W. Jiang, L. A. Marraffini, F. Zhang, Multiplex genome engineering using CRISPR/Cas systems. *Science* **339**, 819–823 (2013). [Medline doi:10.1126/science.1231143](#)
23. B. Nilius, J. Prenen, U. Wissenbach, M. Bödding, G. Droogmans, Differential activation of the volume-sensitive cation channel TRP12 (OTRPC4) and volume-regulated anion currents in HEK-293 cells. *Pflugers Arch.* **443**, 227–233 (2001). [Medline doi:10.1007/s004240100676](#)
24. C. Y. Hernández-Carballo, J. A. De Santiago-Castillo, T. Rosales-Saavedra, P. Pérez-Cornejo, J. Arreola, Control of volume-sensitive chloride channel inactivation by the coupled action of intracellular chloride and extracellular protons. *Pflugers Arch.* **460**, 633–644 (2010). [Medline doi:10.1007/s00424-010-0842-0](#)
25. G. X. Wang, C. McCrudden, Y. P. Dai, B. Horowitz, J. R. Hume, I. A. Yamboliev, Hypotonic activation of volume-sensitive outwardly rectifying chloride channels in cultured PSMCs is modulated by SGK. *Am. J. Physiol. Heart Circ. Physiol.* **287**, H533–H544 (2004). [Medline doi:10.1152/ajpheart.00228.2003](#)
26. J. L. Leaney, S. J. Marsh, D. A. Brown, A swelling-activated chloride current in rat sympathetic neurones. *J. Physiol.* **501**, 555–564 (1997). [Medline doi:10.1111/j.1469-7793.1997.555bm.x](#)
27. G. Smits, A. V. Kajava, LRRC8 extracellular domain is composed of 17 leucine-rich repeats. *Mol. Immunol.* **41**, 561–562 (2004). [Medline doi:10.1016/j.molimm.2004.04.001](#)
28. S. Penuela, R. Gehi, D. W. Laird, The biochemistry and function of pannexin channels. *Biochim. Biophys. Acta* **1828**, 15–22 (2013). [Medline doi:10.1016/j.bbamem.2012.01.017](#)

29. S. Maeda, S. Nakagawa, M. Suga, E. Yamashita, A. Oshima, Y. Fujiyoshi, T. Tsukihara, Structure of the connexin 26 gap junction channel at 3.5 Å resolution. *Nature* **458**, 597–602 (2009). [Medline doi:10.1038/nature07869](#)
30. B. Nilius, J. Sehrer, F. Viana, C. De Greef, L. Raeymaekers, J. Eggermont, G. Droogmans, Volume-activated Cl⁻ currents in different mammalian non-excitabile cell types. *Pflugers Arch.* **428**, 364–371 (1994). [Medline doi:10.1007/BF00724520](#)
31. T. Hayashi, Y. Nozaki, M. Nishizuka, M. Ikawa, S. Osada, M. Imagawa, Factor for adipocyte differentiation 158 gene disruption prevents the body weight gain and insulin resistance induced by a high-fat diet. *Biol. Pharm. Bull.* **34**, 1257–1263 (2011). [Medline doi:10.1248/bpb.34.1257](#)
32. M. Magrane, U. Consortium, UniProt Knowledgebase: A hub of integrated protein data. *Database (Oxford)* **2011**, bar009 (2011). [Medline doi:10.1093/database/bar009](#)
33. T. J. Lopes, M. Schaefer, J. Shoemaker, Y. Matsuoka, J. F. Fontaine, G. Neumann, M. A. Andrade-Navarro, Y. Kawaoka, H. Kitano, Tissue-specific subnetworks and characteristics of publicly available human protein interaction databases. *Bioinformatics* **27**, 2414–2421 (2011). [Medline doi:10.1093/bioinformatics/btr414](#)
34. A. Krogh, B. Larsson, G. von Heijne, E. L. Sonnhammer, Predicting transmembrane protein topology with a hidden Markov model: Application to complete genomes. *J. Mol. Biol.* **305**, 567–580 (2001). [Medline doi:10.1006/jmbi.2000.4315](#)
35. P. Mali, L. Yang, K. M. Esvelt, J. Aach, M. Guell, J. E. DiCarlo, J. E. Norville, G. M. Church, RNA-guided human genome engineering via Cas9. *Science* **339**, 823–826 (2013). [Medline doi:10.1126/science.1232033](#)
36. M. B. Rust, S. L. Alper, Y. Rudhard, B. E. Shmukler, R. Vicente, C. Brugnara, M. Trudel, T. J. Jentsch, C. A. Hübner, Disruption of erythroid K-Cl cotransporters alters erythrocyte volume and partially rescues erythrocyte dehydration in SAD mice. *J. Clin. Invest.* **117**, 1708–1717 (2007). [Medline doi:10.1172/JCI30630](#)
37. S. Arvidsson, M. Kwasniewski, D. M. Riaño-Pachón, B. Mueller-Roeber, QuantPrime—a flexible tool for reliable high-throughput primer design for quantitative PCR. *BMC Bioinformatics* **9**, 465 (2008). [Medline doi:10.1186/1471-2105-9-465](#)
38. J. E. Capó-Aponte, P. Iserovich, P. S. Reinach, Characterization of regulatory volume behavior by fluorescence quenching in human corneal epithelial cells. *J. Membr. Biol.* **207**, 11–22 (2005). [Medline doi:10.1007/s00232-005-0800-5](#)